

Supplementary Information

Programming Biomolecular Self-Assembly Pathways

Peng Yin^{1,2}, Harry M.T. Choi¹, Colby R. Calvert¹ & Niles A. Pierce^{1,3,*}¹Department of Bioengineering, ²Department of Computer Science, ³Department of Applied & Computational Mathematics
California Institute of Technology, Pasadena, CA 91125, USA

*Email: niles@caltech.edu

Contents

S1 Summary figure	1
S2 Reaction graph conventions	2
S3 Catalytic geometry	3
S3.1 System design for catalytic formation of a 3-arm junction	3
S3.2 Execution of the reaction graphs	4
S3.3 Catalytic formation of a 4-arm junction	5
S3.4 AFM image analysis	6
S3.5 Design for the catalytic formation of a k-arm junction	8
S4 Catalytic circuitry	10
S4.1 Execution of the reaction graph	10
S4.2 Detailed secondary structure mechanism	11
S4.3 Stepping gel	13
S4.4 System kinetics analysis	14
S5 Nucleated dendritic growth	16
S5.1 Execution of the reaction graph	16
S5.2 Detailed secondary structure mechanism	17
S5.3 Quantitative amplification gel	19
S5.4 AFM image analysis	20
S6 Autonomous locomotion	23
S6.1 Execution of the reaction graph	23
S6.2 Secondary structure of the walker system	24
S6.3 Detailed secondary structure mechanism	25
S6.4 Assembly of the walker system	27
S6.5 Characterization of the fuel system	29
S6.6 Raw data for the fluorescence quenching experiments	30
S6.7 Statistical analysis	33
S6.8 Comparison of walker time scales	34
S6.9 Control for walker landing effects	36
S7 Discussion	37
S7.1 Leakage and ligation	37
S7.2 Molecular compiler	38
S8 DNA sequences	39
S8.1 Catalytic 3-arm junction system	39
S8.2 Catalytic 4-arm junction system	40
S8.3 Autocatalytic system	42
S8.4 Nucleated dendritic growth system	43
S8.5 Fuel for the walker system	45
S8.6 Walker system	46

S1 Summary figure

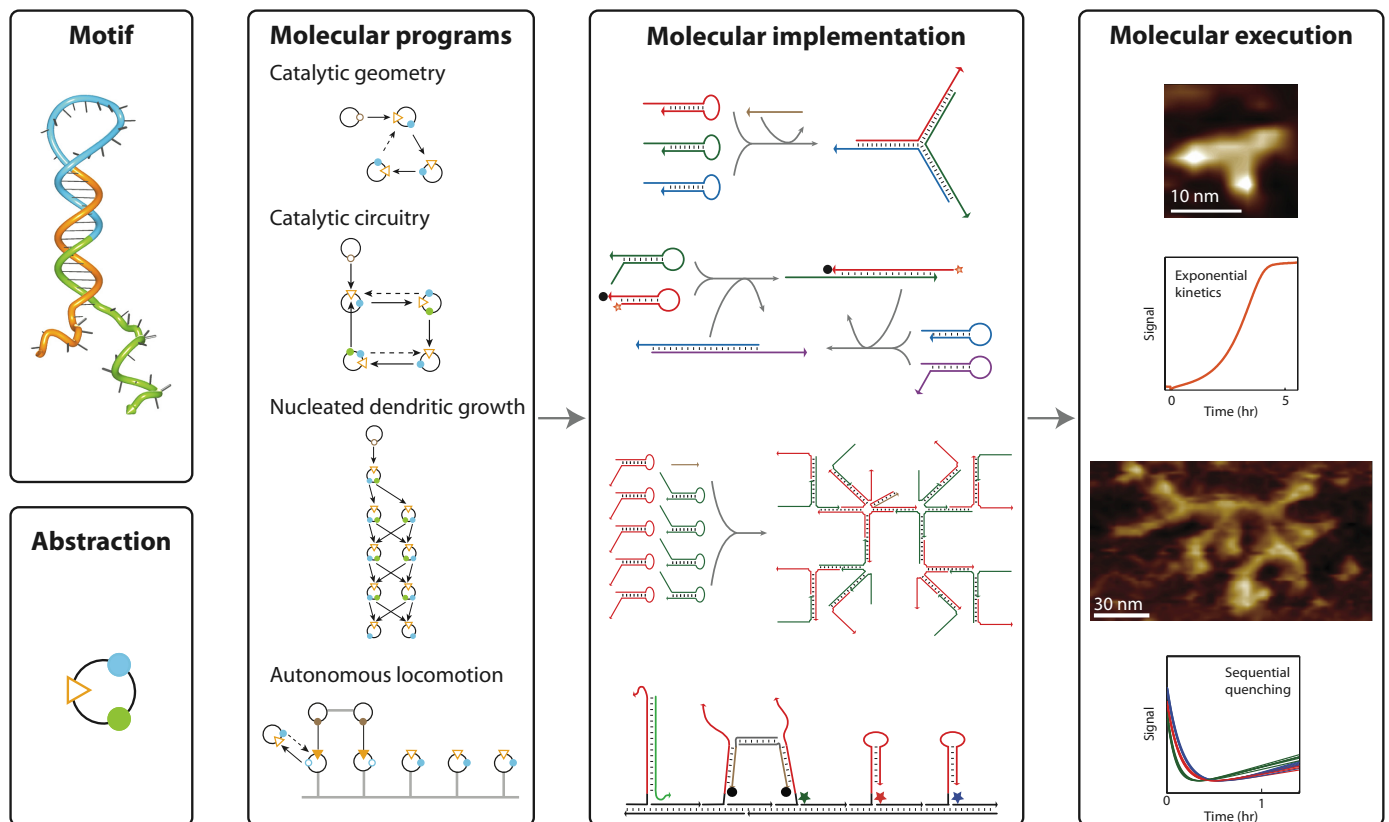


Figure S1. Summary. Diverse biomolecular self-assembly (and disassembly) pathways are programmed using an abstraction of a versatile DNA hairpin motif.

S2 Reaction graph conventions

Using the definitions introduced in the main text, the reaction graph abstraction obeys the following conventions.

Initial conditions

- The initial condition of the system is defined by the state of each port and the initial bonds between the ports.
- An initial bond between an output port and an input port implies that an assembly reaction has already occurred prior to the execution of the reaction graph (see, e.g., the bond between the output port of I and the input port of A in Fig. 5a).

Static structural elements

- Static structural elements are depicted by gray line segments (e.g. the substrate of Fig. 5a) and are inert during execution of the reaction graph.
- These elements can be used to impose geometric constraints on the execution of the reaction graph (e.g. the rigid substrate and inextensible torso of the walker system, Sect. S6.1).

Execution starting points

- Execution begins with any solid arrow (assembly reaction) connecting two accessible ports.
- In a system lacking two accessible ports connected by a solid arrow, execution cannot begin (e.g., the removal of node I prevents execution of all programs described in the present work).

Assembly reaction

- An assembly reaction is depicted by a solid arrow that points from an input port to a complementary output port of a different node.
- An assembly reaction is executed when these two ports are simultaneously accessible.
- In the execution of an assembly reaction, a bond is formed between the two ports, they are flipped to their inaccessible states, and the internal logic of the node with the affected input port is applied to its output ports (e.g., for the present motif, the output ports are flipped to their accessible states).
- Multiple solid arrows entering the same input port depict parallel processes on separate copies of the nodal species (e.g., the input port of node A in Fig. 3a and the input ports of nodes A2-A5 and B2-B5 in Fig. 4a).

Disassembly reaction

- A disassembly reaction is depicted by a dashed arrow that points from an input port to a complementary output port of a different node.
- Using nodal abstractions of the present hairpin motif, a disassembly arrow must complete a *disassembly cycle*. For a cycle involving k nodes: input port 1 \circ blue output port 2 \rightarrow input port 3 \circ blue output port 4 \dots blue output port $2k$ \dashrightarrow input port 1, where \rightarrow denotes an assembly reaction, \dashrightarrow denotes a disassembly reaction, and \circ denotes the internal logical connection between two ports on the same node. For example, Fig. 1d contains a disassembly cycle for $k = 2$: input port of A \circ blue output of A \rightarrow input port of B \circ blue output port of B \dashrightarrow input port of A. Fig. 2a contains a disassembly cycle for $k = 3$: input port of A \circ blue output port of A \rightarrow input port of B \circ blue output port of B \rightarrow input port of C \circ blue output port of C \dashrightarrow input port of A. In physical terms, this corresponds to requiring that the displacing strand and the strand to be displaced emanate as adjacent branches for a k -arm junction, allowing nucleation of the displacement branch migration (e.g., Figs 2b, S4b, and S7b). The special case of $k = 2$ corresponds to standard toehold-mediated strand displacement¹ (e.g., Fig. 1b, where the whole of domain b of hairpin A serves as the toehold).
- A disassembly reaction is executed when the participating output port is accessible and the participating input port is inaccessible (using nodal abstractions of the present motif, the requirement that a disassembly arrow must complete a disassembly cycle implies that the participating output port can only become accessible after the participating input port becomes inaccessible).
- In the execution of a disassembly reaction (e.g., Fig. 1e), the existing bond from an (inaccessible) output port to an (inaccessible) input port is replaced by a new bond to the displacing (accessible) output port; the states of both output ports are flipped.
- Multiple dashed arrows entering the same input port depict parallel disassembly cycles involving separate copies of the nodal species (no such example is presented in this paper).

S3 Catalytic geometry

S3.1 System design for catalytic formation of a 3-arm junction

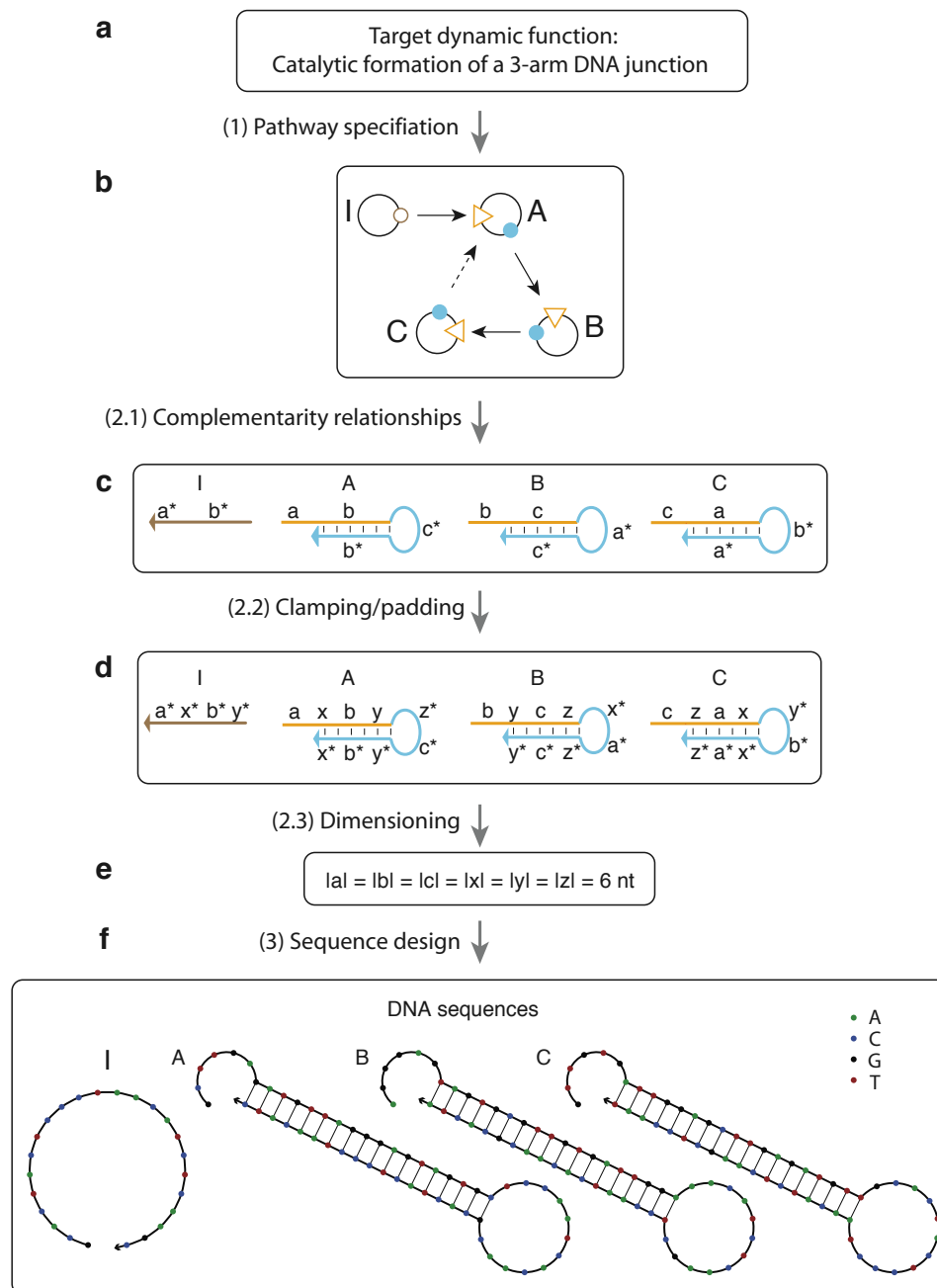


Figure S2. Procedure for designing the catalytic 3-arm junction system.

Here we describe the design procedure for the catalytic 3-arm junction system presented in Fig. 2.

Step (1) *Pathway specification*. The desired dynamic behavior (Fig. S2a) is specified using a reaction graph (Fig. S2b).

Step (2) *Translation into secondary structure motifs*. The reaction graph can be translated directly into secondary structure motifs.

Step (2.1) *Basic complementarity relationships*. In the reaction graph, two ports connected by an arrow are complementary to each other. These portal complementarity relationships specify the complementarity relationships between the motif

domains modeled by the ports, and thus enable a direct translation of the reaction graph to the secondary structure motifs (Fig. S2c). For example, the assembly arrow connecting the brown output port of node I and the orange input port of node A (Fig. S2b) indicates these two ports are complementary, and hence the initiator and the orange domain of hairpin A in Fig. S2c are complementary. Similarly, the disassembly arrow connecting the blue output port of node C and the orange input port of node A (Fig. S2b) indicates these two ports are complementary, and hence the blue domain of hairpin C is complementary to the orange domain of hairpin A in Fig. S2c.

Step (2.2) Clamping/padding. The basic implementation (Fig. S2c) is modified by adding clamping/padding segments (x , y , z , x^* , y^* , and z^* in Fig. S2d). These segments serve two purposes. First, they serve as ‘padding’ segments to modulate the lengths of a hairpin’s sticky-end, stem, and loop regions, permitting more flexible dimensioning in Step (2.3). Second, the segments serve as ‘clamps’ to decrease spurious ‘leakage’ reactions in the absence of the initiators. Consider *un-clamped* hairpin A and hairpin B in Fig. S2c. When the left-end of the stem of hairpin A ‘breathes’, the 3’ end of segment b^* will be transiently exposed, revealing a partial toehold that is complementary to the toehold b of hairpin B. This transient toehold exposure would permit hairpin A and hairpin B to react spuriously and form A·B (which would then react with C to form A·B·C). By contrast, the ‘breathing’ of the left end of the *clamped* hairpin A stem in Fig. S2d exposes x^* instead of b^* . Thus, b^* remains sequestered, discouraging spurious nucleation between A and B at b^* .

Step (2.3) Segment dimensioning. The purpose of segment dimensioning is to assign the length of each segment (number of nucleotides) such that under specified conditions, spurious reactions are suppressed and the desired reaction proceeds smoothly. The NUPACK server (www.nupack.org) is used for dimensioning. For the catalytic 3-arm junction system described here, the thermodynamic analysis of the interacting DNA strands suggests that assigning 6-nt to each segment (Fig. S2e) stabilizes critical structures in the reaction pathway in the context of a dilute solution of interacting nucleic acid strands.

Step (3) Sequence design. See Methods in main text.

S3.2 Execution of the reaction graphs

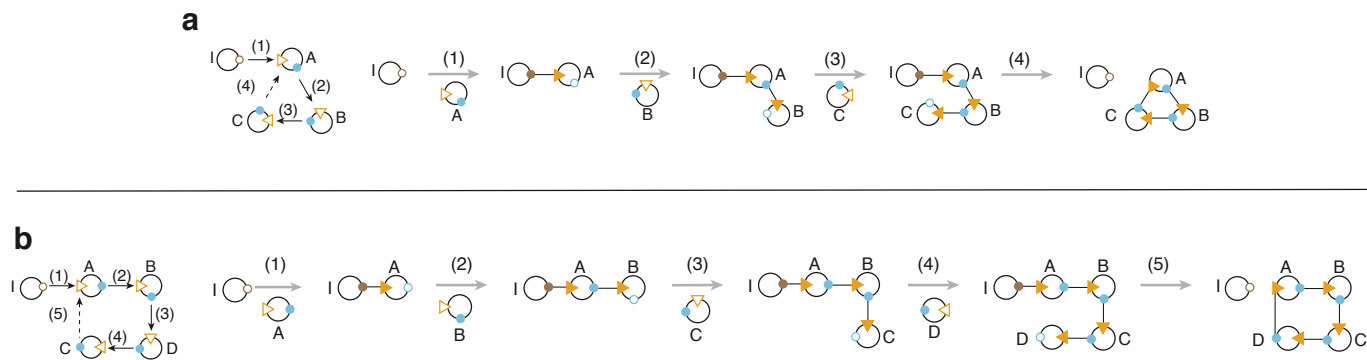


Figure S3. Execution of reaction graphs for catalytic 3-arm/4-arm junction systems. **a**, Execution of the reaction graph of Fig. 2a. Reaction 1 (assembly): A bond is made between the accessible output port of I and the accessible input port of A and both ports are flipped to inaccessible states; the output port of A is flipped to the accessible state (based on the internal logic of node A). Reaction 2 (assembly): A bond is made between the newly accessible output port of A and the accessible input port of B and both ports are flipped to inaccessible states; the output port of B is flipped to the accessible state (based on the internal logic of node B). Reaction 3 (assembly): A bond is made between the newly accessible output port of B and the input port of C and both ports are flipped to inaccessible states; the output port of C is flipped to the accessible state (based on the internal logic of node C). Reaction 4 (disassembly): The bond between the inaccessible output port of I and the inaccessible input port of A is displaced by a bond between the newly accessible blue output port of C and the input port of A; the states of the two output ports are flipped. **b**, Execution of the reaction graph of Fig. 2e.

Fig. S3 depicts the step-by-step execution of the reaction graphs in Figs 2a and e. Note that the reaction graph in Fig. S3a contains a $k = 3$ disassembly cycle: input port of A \circ blue output port of A \rightarrow input port of B \circ blue output port of B \rightarrow input port of C \circ blue output port of C \rightarrow input port of A; the reaction graph in Fig. S3b contains a $k = 4$ disassembly cycle: input port of A \circ blue output port of A \rightarrow input port of B \circ blue output port of B \rightarrow input port of C \circ blue output port of C \rightarrow input port of D \circ blue output port of D \rightarrow input port of A.

S3.3 Catalytic formation of a 4-arm junction

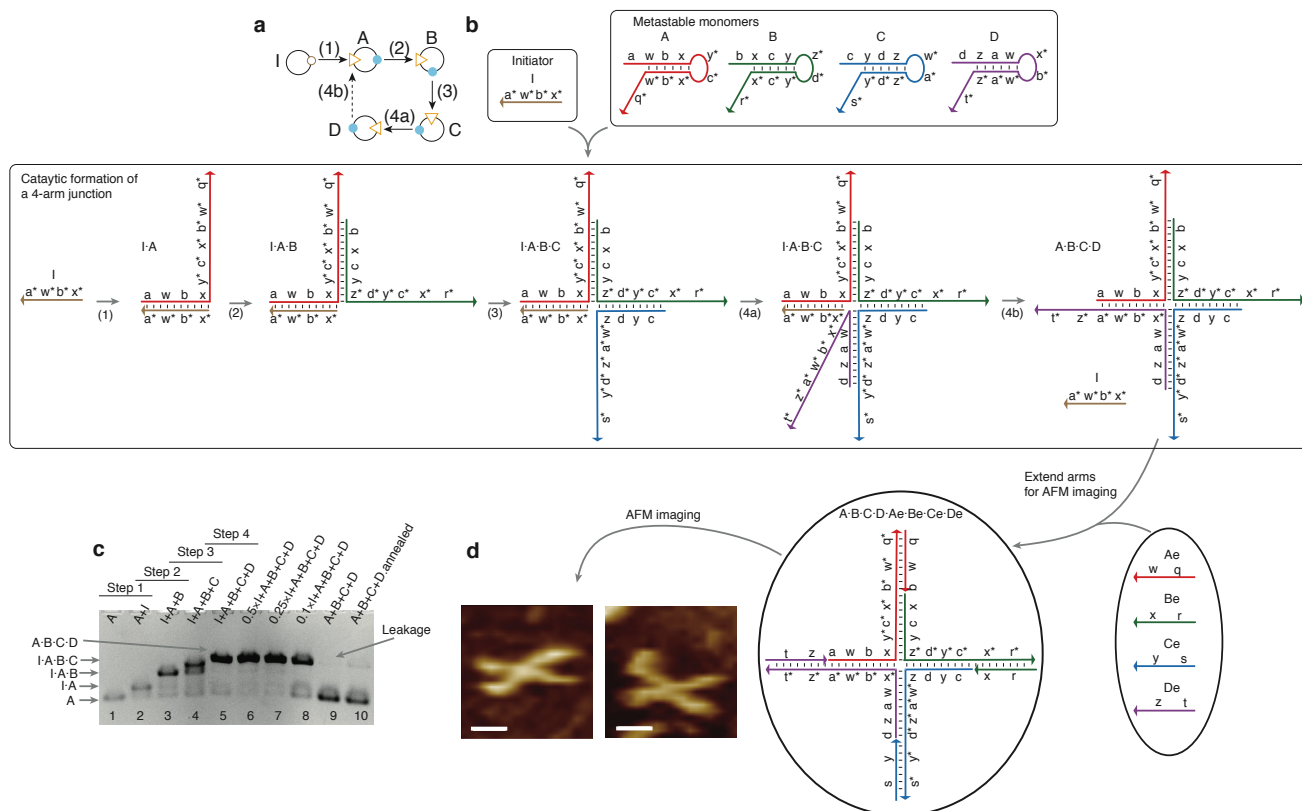


Figure S4. Catalytic formation of a 4-arm DNA junction. **a**, Reaction graph. Note that since the green output ports do not serve as initiators for any downstream reaction, they are omitted here for simplicity. See Sect. S3.2 for step-by-step execution of the graph. **b**, Secondary structure schematic of the reaction. The lengths of segments q, q*, r, r*, s, s*, t, and t* are 18 nt; the lengths of the other segments are 6 nt. Hairpins A, B, C, and D are metastable in the absence of the initiator I. The initiator I catalyzes monomers A, B, C, and D to form a 4-arm DNA junction, as follows: (1) segment a* of I nucleates at the toehold a of hairpin A and initiates a strand displacement that results in the opening of hairpin A; (2) newly exposed b* of A nucleates at toehold b of B and results in the opening of B; (3) newly exposed c* of B nucleates at toehold c of C and results in the opening of C; (4a) newly exposed d* of C nucleates at d of hairpin D and results in the opening of D; (4b) D displaces I from A. **c**, Agarose gel electrophoresis demonstrates the catalytic formation of the 4-arm junction. Lanes 1-5: A gel shifting assay validates each reaction step depicted in panel (b). Lanes 5-9: Effects of different concentrations of I (1×, 0.5×, 0.25×, 0.1×, and 0×) on the formation of A·B·C·D. 600 nM reactants were incubated at room temperature for 2 hours. Lane 10: A·B·C·D annealed over 2.5 hours (600 nM hairpin species heated at 95 °C for 5 minutes and cooled to room temperature over 2.5 hrs). The 2% agarose gel was prepared in 1× LB buffer (Faster Better Media, LLC) with 0.5 μg/ml ethidium bromide. The gels were run at 150 V for 30 min at room temperature and then visualized using UV transillumination. The hairpins used for these reactions did not contain the 3' tails (q*, r*, s*, and t*). **d**, AFM images of two 4-arm junctions. To assist in AFM imaging of the 4-arm junction, four strands (Ae, Be, Ce, and De) were incubated with the catalytically formed 4-arm junction A·B·C·D. Note that the duplex portion of the arms of the final structure A·B·C·D·Ae·Be·Ce·De are twice as long as the duplex portion of the arms of A·B·C·D. Two AFM images of A·B·C·D·Ae·Be·Ce·De are presented. Scale bar, 10 nm. See Sect. S3.4 for length measurements.

Fig. S4a and b depict the reaction graph and reaction schematic for the catalytic formation of a 4-arm junction. In the absence of initiator I, hairpins A, B, C, and D are kinetically impeded from forming the 4-arm junction that is predicted to dominate at equilibrium. Introduction of I into the system (Fig. S4b, bottom) activates a cascade of assembly steps with A, B, C, and D followed by a disassembly step in which D displaces I from the complex, freeing I to catalyze the self-assembly of additional branched junctions.

Native agarose gel electrophoresis (Fig. S4c) confirms that the hairpins assemble slowly in the absence of the initiator (Lane 9) and that assembly is dramatically accelerated by the addition of initiator (Lane 5). Disassembly of the initiator enables catalytic turnover as indicated by the nearly complete consumption of hairpins even at sub-stoichiometric initiator concentrations (Lanes 6-8). As in the 3-arm junction case, only minimal assembly is achieved by annealing the hairpin mixture (Lane 10).

AFM imaging of the catalyzed self-assembly product (augmented with strands that extend the duplex portion of each arm as described in the caption) reveals the expected 4-arm junction morphology (Fig. S4d).

S3.4 AFM image analysis

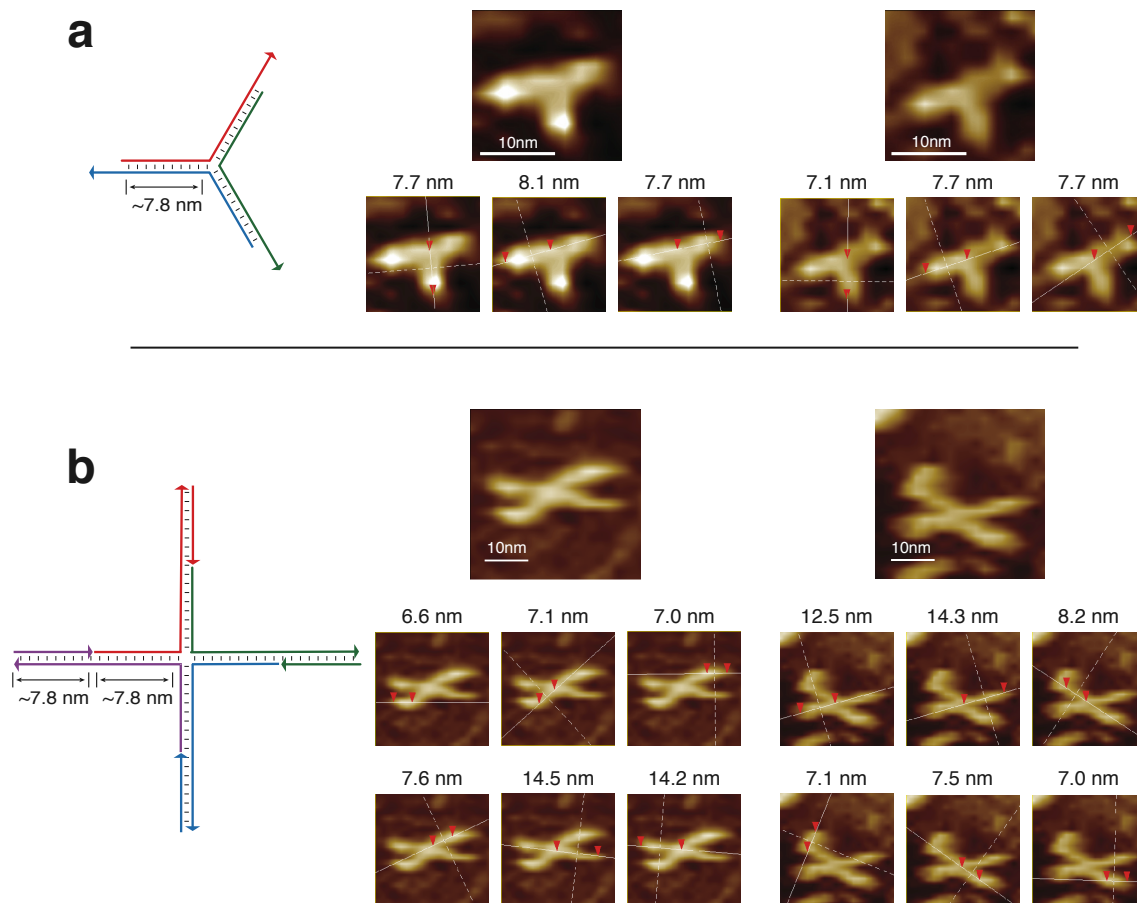


Figure S5. AFM image analysis of 3-arm/4-arm junctions. AFM measurements of the 3-arm (panel a) and 4-arm (panel b) junctions described in Fig. 2 and Fig. S4. The small images are screenshots of the measurement section files. The distance between the two arrows is listed above the image.

Using a B-DNA model where one helical turn contains 10.5 base pairs and measures 3.4 nm, we calculate the expected arm length for the 3-arm junction as follows: $(24 / 10.5) \times 3.4 \text{ nm} = 7.8 \text{ nm}$. Similarly, the arm length for the 4-arm junction is calculated to be $7.8 + 7.8 = 15.6 \text{ nm}$. The measured lengths of the arms are roughly consistent with the calculated lengths (Fig. S5). Fig. S6 shows AFM images with a larger field of view for 3-arm (panel a) and 4-arm (panel b) junctions.

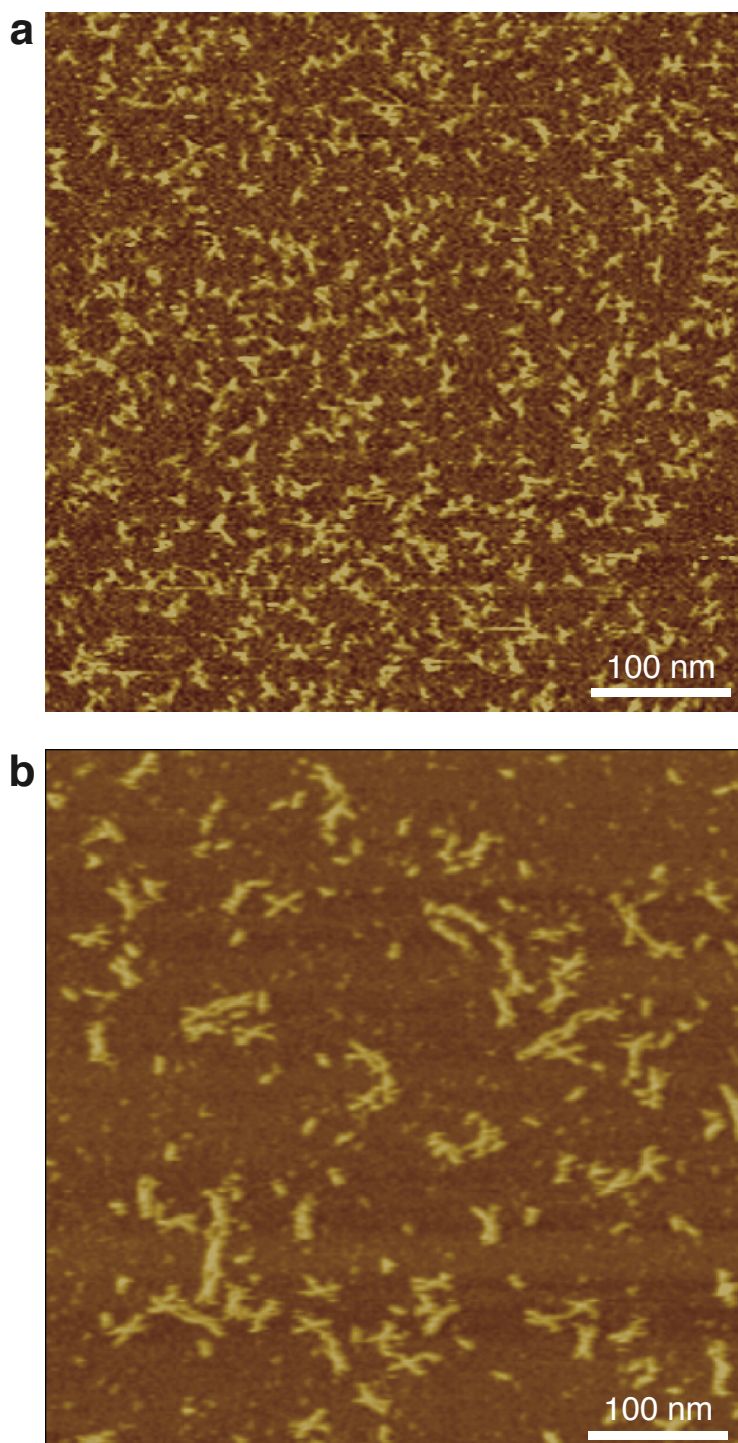


Figure S6. Large-field-of-view AFM images of the 3-arm (a) and 4-arm (b) junction systems.

S3.5 Design for the catalytic formation of a k-arm junction

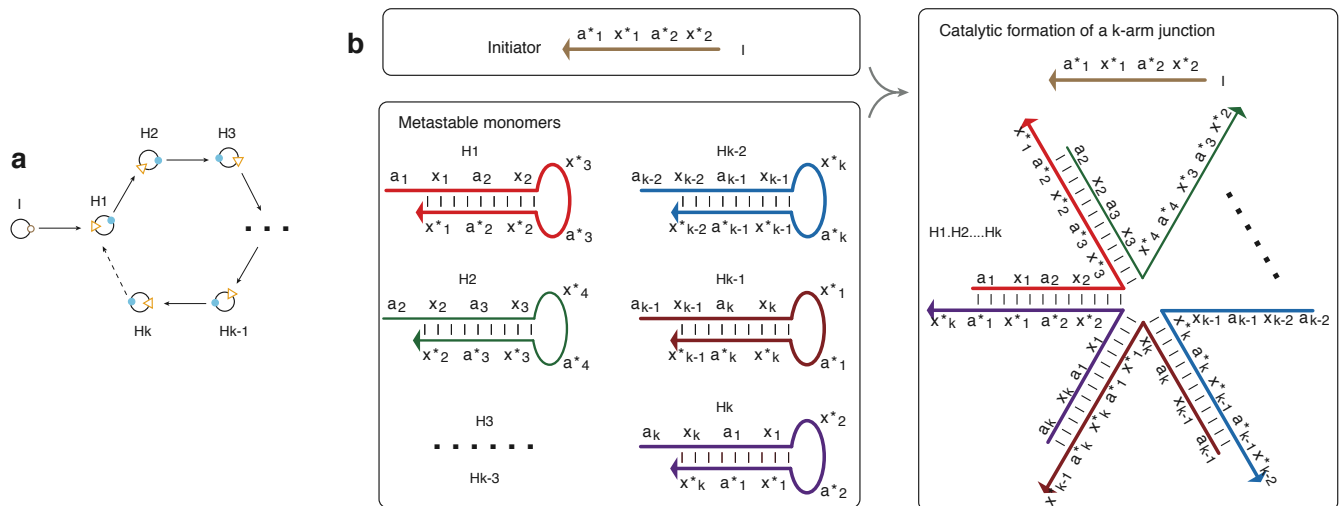


Figure S7. Catalytic formation of a k-arm junction. **a**, Reaction graph. **b**, Reaction schematics. Hairpins H_1, H_2, \dots, H_k are metastable in the absence of the initiator I . The initiator I catalyzes monomers H_1, H_2, \dots, H_k to form a k-arm DNA junction.

The catalytic system described in Fig. 2 and Fig. S4 can, in principle, be generalized to a system capable of the catalytic formation of a k-arm junction. Fig. S7 describes the reaction graph and the secondary structure schematic for the catalytic formation of a k-arm junction. Fig. S8 gives an example when $k = 6$.

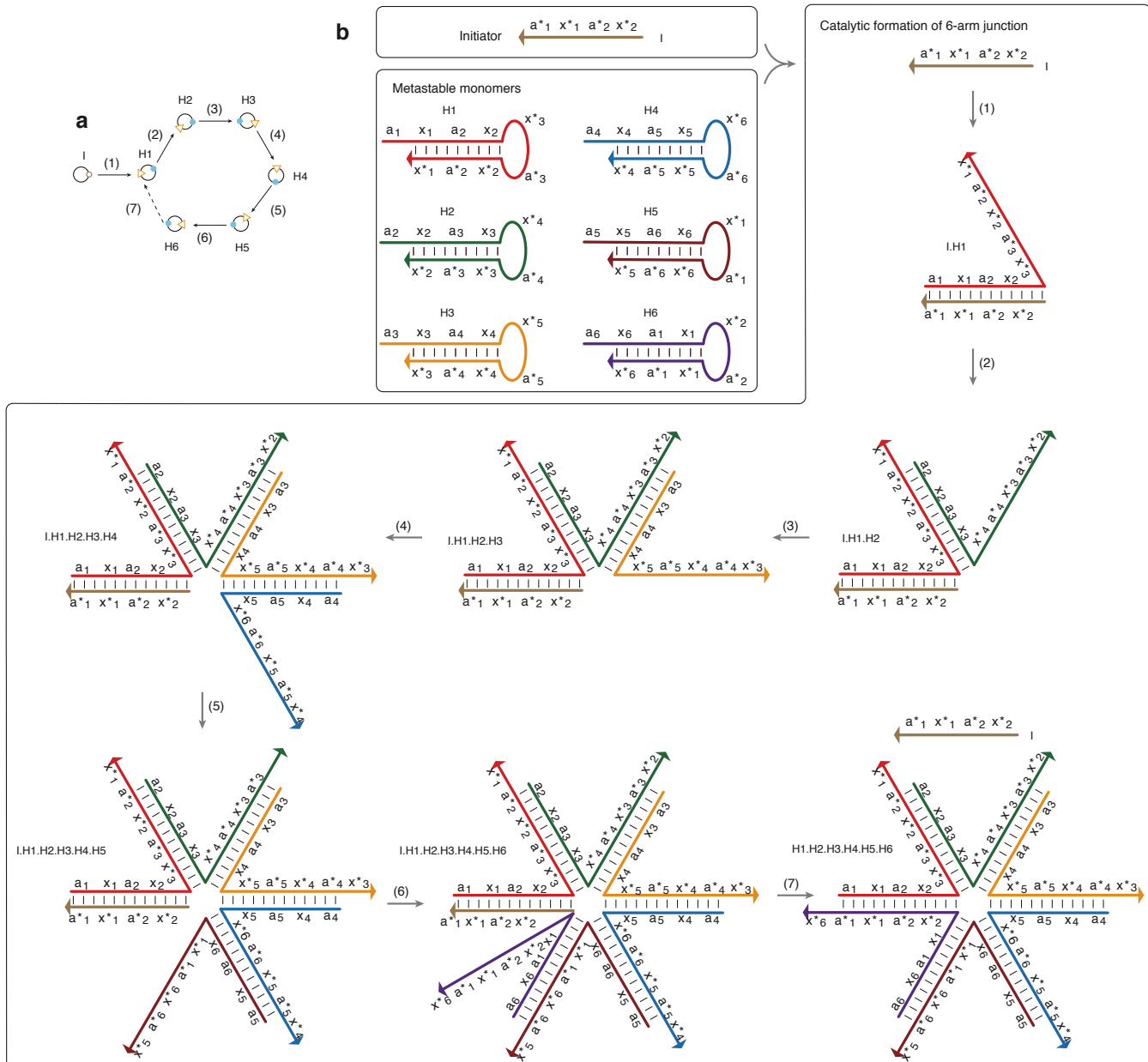


Figure S8. Catalytic formation of a 6-arm junction. **a**, Reaction graph. **b**, Step-by-step reaction schematic. Hairpins H₁, H₂, H₃, H₄, H₅, and H₆ are metastable in the absence of the initiator I. The initiator I catalyzes monomers H₁, H₂, H₃, H₄, H₅, and H₆ to form a 6-arm DNA junction as follows. Step 1: segment a_1^* of I nucleates at the toehold a_1 of hairpin H₁ and initiates a strand displacement that results in the opening of hairpin H₁. Step 2: the newly exposed a_2^* of H₁ nucleates at the toehold a_2 of hairpin H₂ and opens hairpin H₂. Step 3: the newly exposed a_3^* of H₂ nucleates at the toehold a_3 of hairpin H₃ and opens hairpin H₃. Step 4: the newly exposed a_4^* of H₃ nucleates at the toehold a_4 of hairpin H₄ and opens hairpin H₄. Step 5: the newly exposed a_5^* of H₄ nucleates at the toehold a_5 of hairpin H₅ and opens hairpin H₅. Step 6: the newly exposed a_6^* of H₅ nucleates at the toehold a_6 of hairpin H₆ and opens hairpin H₆. Step 7: H₆ displaces I from H₁.

S4 Catalytic circuitry

S4.1 Execution of the reaction graph

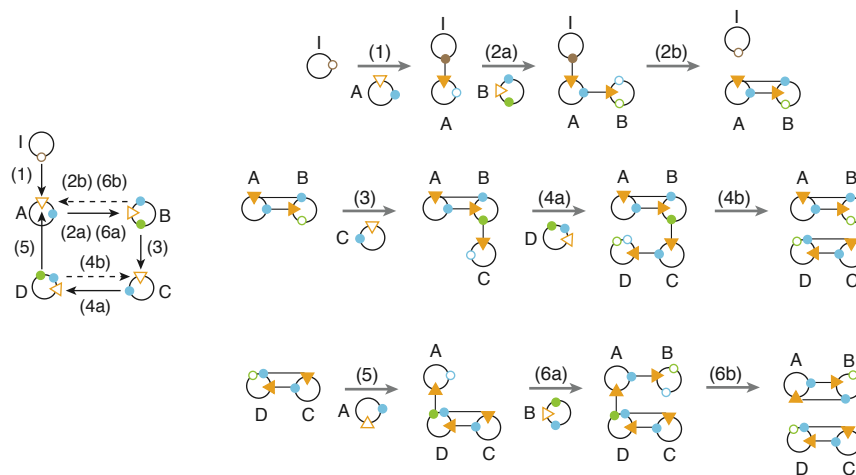


Figure S9. Execution of the reaction graph for the autocatalytic system of Fig. 3.

Fig. S9 describes the step-by-step execution of the reaction in Fig. 3a. The reaction starts at solid arrow (1) that connects the accessible output port of I and the accessible input port of A. Note that by convention, the two arrows entering the same input port of A depict parallel processes on separate copies of the nodal species.

- **Reaction 1 (assembly):** A bond is made between the accessible output port of I and the accessible input port of A and both ports are flipped to inaccessible states; the output port of A is flipped to the accessible state (based on the internal logic of node A).
- **Reaction 2a (assembly):** A bond is made between the newly accessible output port of A and the accessible input port of B and both ports are flipped to inaccessible states; the two output ports of B are flipped to accessible states (based on the internal logic of node B).
- **Reaction 2b (disassembly):** The bond between the inaccessible output port of I and the inaccessible input port of A is displaced by a bond between the newly accessible blue output port of B and the input port of A; the states of the two output ports are flipped.
- **Reaction 3 (assembly):** A bond is made between the newly accessible green output port of B and the accessible input port of C and both ports are flipped to inaccessible states; the output port of C is flipped to the accessible state (based on the internal logic of node C).
- **Reaction 4a (assembly):** A bond is made between the newly accessible output port of C and the accessible input port of D and both ports are flipped to inaccessible states; the output ports of D are flipped to accessible states (based on the internal logic of node D).
- **Reaction 4b (disassembly):** The bond between the inaccessible green output port of B and the inaccessible input port of C is displaced by a bond between the newly accessible blue output port of D and the input port of C; the states of the two output ports are flipped.
- **Reaction 5 (assembly):** A bond is made between the newly accessible green output port of D and the accessible input port of A and both ports are flipped to inaccessible states; the output port of A is flipped to the accessible state (based on the internal logic of node A).
- **Reaction 6a (assembly):** A bond is made between the newly accessible output port of A and the accessible input port of B and both ports are flipped to inaccessible states; the output ports of B are flipped to accessible states (based on the internal logic of node B).
- **Reaction 6b (disassembly):** The bond between the inaccessible green output port of D and the inaccessible input port of A is displaced by a bond between the newly accessible blue output port of B and the input port of A; the states of the two output ports are flipped.

S4.2 Detailed secondary structure mechanism

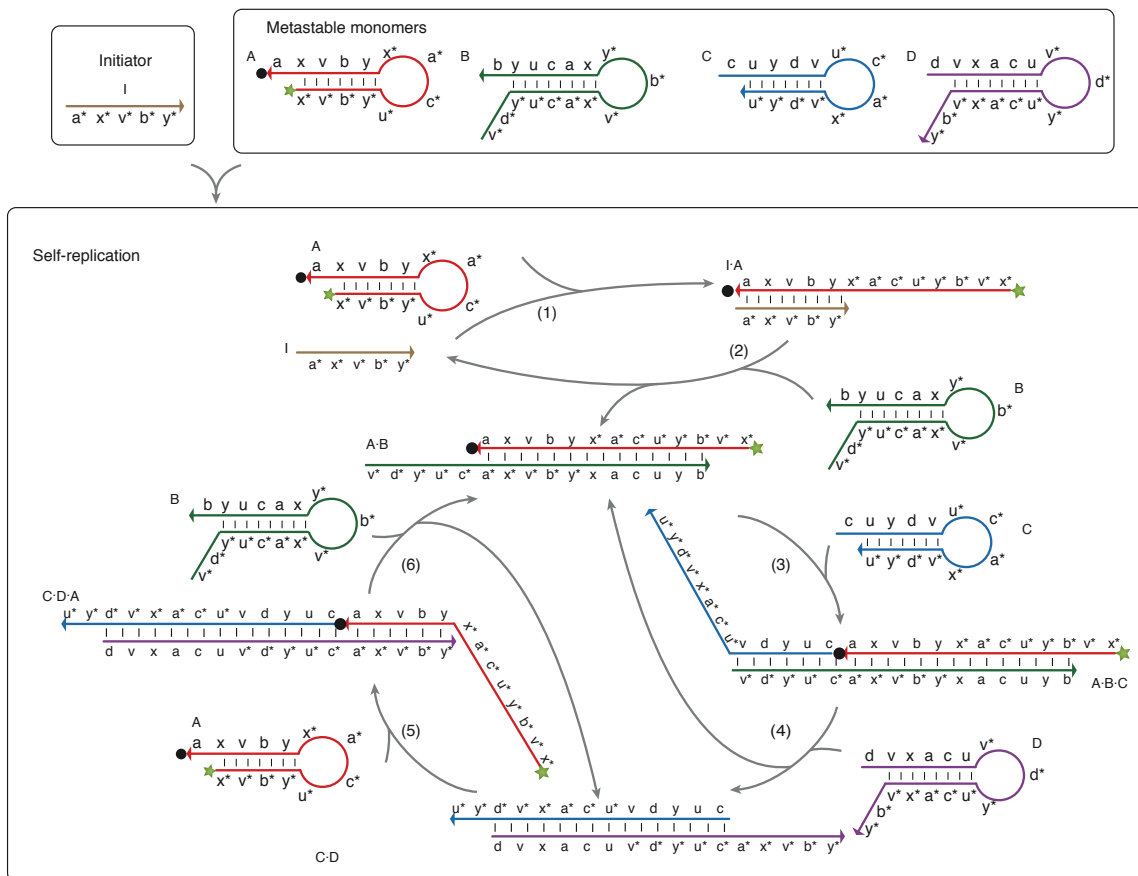


Figure S10. Detailed reaction schematic for the autocatalytic system of Fig. 3. The length of each segment is 6 nt. Green star, fluorophore; black dot, quencher.

Fig. S10 describes the detailed reaction flow of the autocatalytic system described in Fig. 3. Fig. S11 describes additional intermediate steps. Steps 1-2 are the initiation stage; steps 3-6 are the exponential amplification stage.

- Step 1: the toehold a^* of I nucleates at the toehold a of A, resulting in the opening of the hairpin and the formation of the product I·A.
- Step 2: I·A, with b^* newly exposed, opens hairpin B (step 2a); B subsequently displaces I from A (step 2b), producing A·B and bringing the system to the exponential amplification stage. The single-stranded tail ($v^*-d^*-y^*-u^*-c^*$) of A·B next catalyzes C and D to form C·D (in steps 3 and 4).
- Step 3: A·B, with c^* newly exposed, opens hairpin C.
- Step 4: A·B·C, with d^* newly exposed, opens hairpin D (step 4a); D subsequently displaces C from B, separating A·B and C·D (step 4b). The single-stranded tail ($a^*-x^*-v^*-b^*-y^*$) of C·D is identical to I and next catalyzes A and B to form A·B (in steps 5 and 6).
- Step 5: C·D, with a^* newly exposed, opens hairpin A.
- Step 6: C·D·A, with b^* newly exposed, opens B (step 6a); B subsequently displaces A from D, separating C·D and A·B (step 6b).

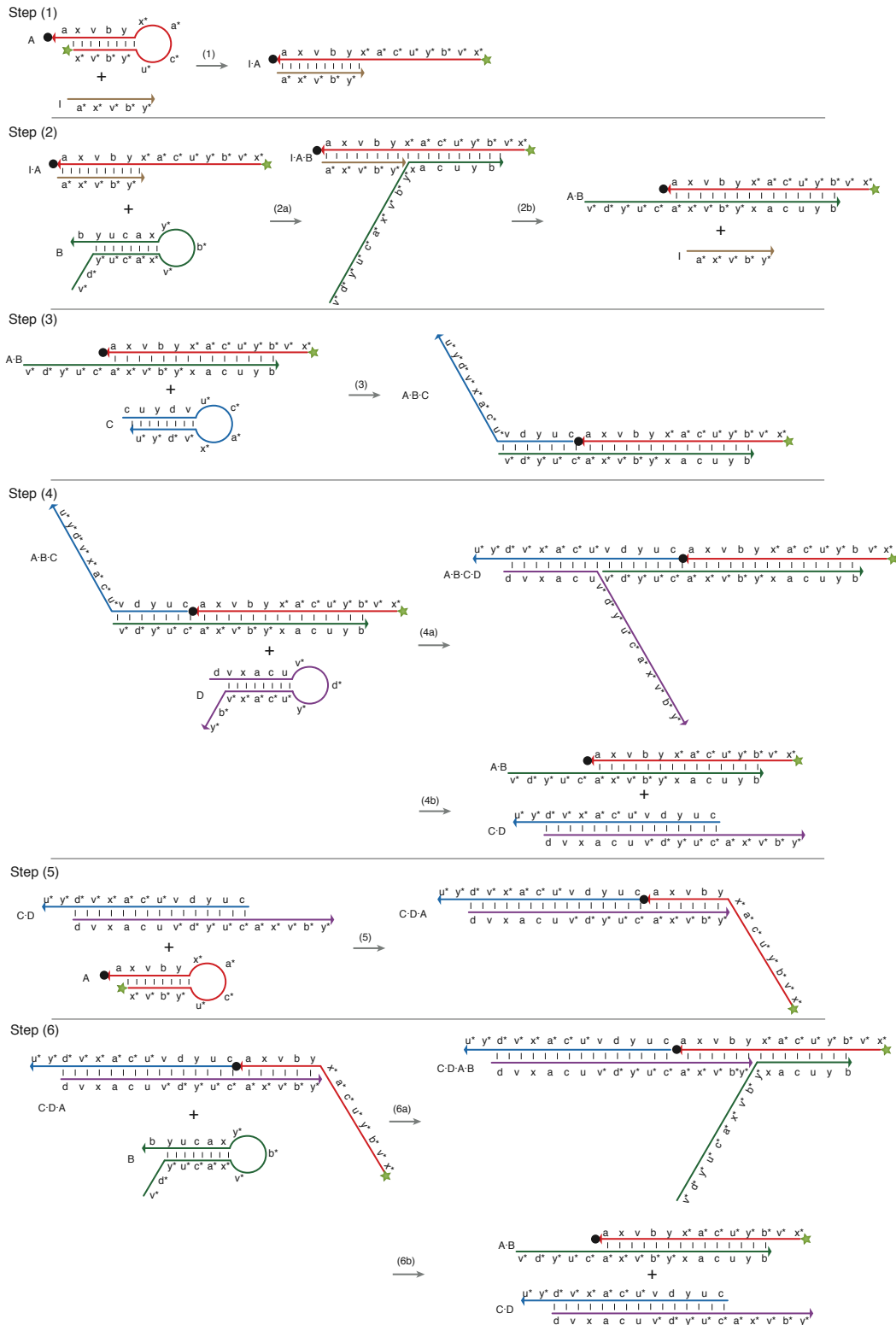


Figure S11. Step-by-step reaction schematic for the autocatalytic system of Fig. 3.

S4.3 Stepping gel

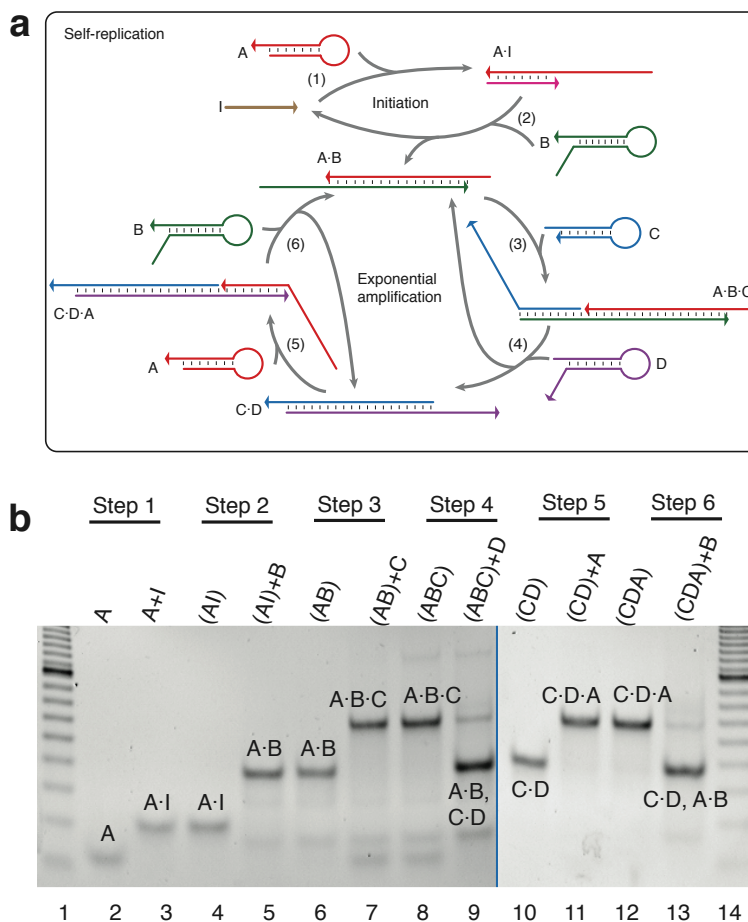


Figure S12. Stepping gel for the autocatalytic system. **a**, Reaction schematic. **b**, Native polyacrylamide gel electrophoresis demonstrates the step-by-step reaction depicted in Fig. 3b. The symbol () indicates annealing; + indicates 15 minute reaction at room temperature. The hairpins used for these reactions were synthesized and purified by IDT DNA and used without further purification. The annealed samples were annealed at 2 μM reactant concentrations: heating at 95 $^{\circ}\text{C}$ for 5 minutes followed by cooling to room temperature over approximately 2.5 hours. The room temperature reactions were conducted with each reactant species at 1 μM concentration. Consider the sample, (AI) + B, in Lane 5. The sample was prepared by first annealing a mix containing 2 μM A and 2 μM I to produce (AI). Then 2 μL of (AI), at 2 μM concentration, was mixed with 2 μL of B at 2 μM concentration and allowed to react at room temperature for 15 minutes. Lanes 1 and 14 are 20-1000 bp DNA ladders (Bio-Rad). The 5% native polyacrylamide gel was prepared in 1 \times TAE/Mg⁺⁺ buffer (20 mM Tris, pH = 7.6, 2 mM EDTA, 12.5 mM Mg⁺⁺). The samples were loaded with 10% glycerol. The gel was run at 100 V for 90 minutes at room temperature, post-stained with 0.5 $\mu\text{g}/\text{mL}$ ethidium bromide, and visualized by UV transillumination. The blue line delineates the boundary between two gels.

The autocatalytic system was validated on a step-by-step basis using native polyacrylamide gel electrophoresis (PAGE) (Fig. S12):

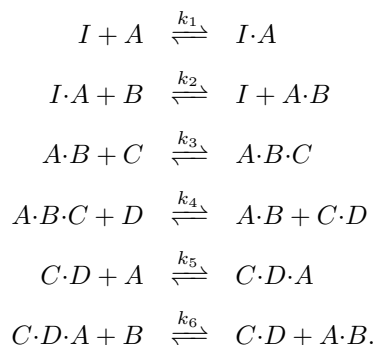
- Step 1. Hairpin A reacts with initiator I and produces a band that corresponds to product A-I (Lane 3), which migrates at about the same speed as the annealed product A-I (Lane 4), as expected.
- Step 2. Annealed sample A-I reacts with hairpin B and produces a band that corresponds to product A-B (Lane 5), which migrates at about the same speed as the annealed product A-B (Lane 6), as expected.
- Step 3. Annealed sample A-B reacts with hairpin C and produces a band that corresponds to product A-B-C (Lane 7), which migrates at about the same speed as the annealed product A-B-C (Lane 8), as expected.
- Step 4. Annealed sample A-B-C reacts with hairpin D and produces a band that corresponds to product A-B and C-D (Lane 9), which migrates at about the same speed as the annealed product A-B (Lane 6) and the annealed product C-D (Lane 10), as expected.
- Step 5. Annealed sample C-D reacts with hairpin A and produces a band that corresponds to product C-D-A (Lane 11), which migrates at about the same speed as the annealed product C-D-A (Lane 12), as expected.

- Step 6. Annealed sample C·D·A reacts with hairpin B and produces a band that corresponds to product C·D and A·B (Lane 13), which migrates at about the same speed as the annealed product C·D (Lane 10) and the annealed product A·B (Lane 6), as expected.

S4.4 System kinetics analysis

Analytical modeling

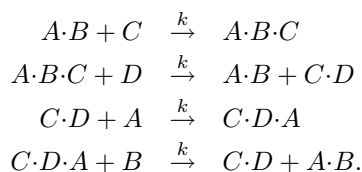
The autocatalytic system is modeled using the following reactions:



To make the system tractable for analytical treatment, we make the following simplifying assumptions:

- *Assumption 1.* The forward reaction rates are all the same: $k_i = k$, for $i = 1, \dots, 6$. This is based on the fact that all the reactions are strand-displacement reactions mediated by 6-nt toe-holds. Under the experimental conditions, the rate limiting step of the toe-hold mediated reactions is the nucleation step,² the rate of which is determined primarily by the toe-hold length.
- *Assumption 2.* The reactions are irreversible. This approximation is justified by the fact that at 25 °C, the equilibrium constants for these reactions (e.g., $K_1 \equiv \frac{Q_{I \cdot A}}{Q_I Q_A}$ for the first equation – here, Q denotes the partition function for a given complex species) are all calculated to be greater than 10^9 using multi-stranded partition function analysis³ with NUPACK (www.nupack.org).
- *Assumption 3.* C·D and I are treated as identical species at the level of mass action kinetics modeled here. This is based on the fact that the active catalytic segment of C·D is identical in sequence to I (see Fig. S10).

Under the above assumptions, the model may be simplified to



The kinetics of the system can be modeled by the following equations:

$$\begin{aligned}
 \frac{d[A \cdot B \cdot C]}{dt} &= k[A \cdot B][C] - k[A \cdot B \cdot C][D] \\
 \frac{d[C \cdot D \cdot A]}{dt} &= k[C \cdot D][A] - k[C \cdot D \cdot A][B] \\
 \frac{d[A \cdot B]}{dt} &= k[A \cdot B \cdot C][D] + k[C \cdot D \cdot A][B] - k[A \cdot B][C] \\
 \frac{d[C \cdot D]}{dt} &= k[A \cdot B \cdot C][D] + k[C \cdot D \cdot A][B] - k[C \cdot D][A].
 \end{aligned}$$

We next analyze the initial reaction stage of the system when the hairpin reactant depletion is small.

- *Assumption 4.* Initial stage assumption. $[A] = [A]_0 = [B] = [B]_0 = [C] = [C]_0 = [D] = [D]_0 = c_0$.

Let $\kappa = k[A]_0 = k[B]_0 = k[C]_0 = k[D]_0 = kc_0$. Solving the above equations under the initial condition, $[A \cdot B]_0 = [C \cdot D \cdot A]_0 = [A \cdot B \cdot C]_0 = 0$ and $[C \cdot D]_0 = [I]_0$, we find

$$\begin{aligned} [A \cdot B \cdot C] &= \frac{1}{8}[I]_0 e^{-\kappa t} (\sqrt{2} e^{\sqrt{2}\kappa t} (1 - e^{-2\sqrt{2}\kappa t}) - 4\kappa t) \\ [C \cdot D \cdot A] &= \frac{1}{8}[I]_0 e^{-\kappa t} (\sqrt{2} e^{\sqrt{2}\kappa t} (1 - e^{-2\sqrt{2}\kappa t}) + 4\kappa t) \\ [A \cdot B] &= \frac{1}{4}[I]_0 e^{-\kappa t} (e^{\sqrt{2}\kappa t} (1 + e^{-2\sqrt{2}\kappa t}) - 2) \\ [C \cdot D] &= \frac{1}{4}[I]_0 e^{-\kappa t} (e^{\sqrt{2}\kappa t} (1 + e^{-2\sqrt{2}\kappa t}) + 2). \end{aligned}$$

Denoting by f the measurable fluorescent species, we have

$$\begin{aligned} f &= [A \cdot B \cdot C] + [C \cdot D \cdot A] + [A \cdot B] \\ &= \frac{1}{4}[I]_0 e^{-\kappa t} (\sqrt{2} e^{\sqrt{2}\kappa t} (1 - e^{-2\sqrt{2}\kappa t})) + \frac{1}{4}[I]_0 e^{-\kappa t} (e^{\sqrt{2}\kappa t} (1 + e^{-2\sqrt{2}\kappa t}) - 2). \end{aligned}$$

For the 6-nt toe-hold mediated strand displacement reactions analyzed here, the reaction constant k is estimated⁴ to be $1 \times 10^5 \text{ M}^{-1}\text{s}^{-1}$. For $c_0 = 20 \text{ nM}$, we have $\kappa = 2 \times 10^{-3}\text{s}^{-1}$. When $t \geq 815 \text{ s}$, we have $e^{\sqrt{2}\kappa t} > 10 \gg 1 \gg 0.1 > e^{-\sqrt{2}\kappa t}$, so the above equation may be simplified to

$$\begin{aligned} f &\approx \frac{\sqrt{2}}{4}[I]_0 e^{-\kappa t} e^{\sqrt{2}\kappa t} + \frac{1}{4}[I]_0 e^{-\kappa t} e^{\sqrt{2}\kappa t} \\ &= \frac{1 + \sqrt{2}}{4}[I]_0 e^{(\sqrt{2}-1)\kappa t}. \end{aligned}$$

This implies that the time, t , required to achieve a given fluorescence level, f , is log-linear in $[I]_0$.

Data analysis

The analytical prediction that there is a regime in which t is log-linear in $[I]_0$ is experimentally verified by the linear fit of the 10% completion time against the logarithm of the relative concentration of I, $0.003 \times \leq [I] \leq 0.05 \times$ (Fig. 3c, inset; Fig. S13, blue circles). High concentration end points ($[I] \geq 0.1 \times$) are excluded based on theoretical analysis ($t \geq 815 \text{ s}$).¹ The low concentration end points ($[I] \leq 0.001 \times$) are excluded due to signal poisoning by leakage. A system with no leakage would be expected to maintain the linear regime to arbitrarily low initiator concentrations. We can model our leaky system by augmenting the initiator concentration $[I]$ by an additional leakage term to obtain an effective concentration, $[I]_{\text{eff}} = [I] + [I]_{\text{leak}}$. With $[I]_{\text{leak}} = 0.005 \times$, a linear regime is observed between the 10% completion time and the logarithm of $[I]_{\text{eff}}$ for $[I] \leq 0.05 \times$ (Fig. S13, red diamonds).

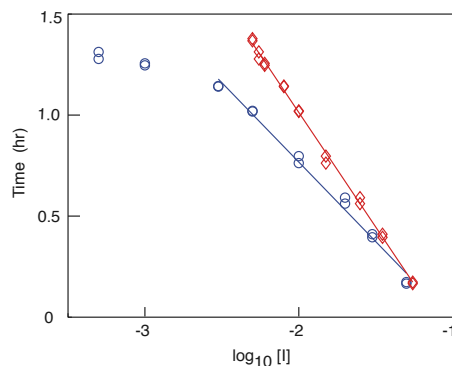


Figure S13. Linear fit of the 10% completion time against the logarithm of the relative concentration of I. Blue circles represent the initiator concentration, $[I]$ (Note that $[I] = 0$ is not shown); red diamonds represent the effective concentration of the initiator, $[I]_{\text{eff}} = [I] + [I]_{\text{leak}}$ with $[I]_{\text{leak}} = 0.005 \times$.

¹The 10% completion time for $[I] = 0.05 \times$ is $610 < 815 \text{ s}$. This data point is nonetheless included: $e^{\sqrt{2}\kappa t} = 5.61$ for $t = 610 \text{ s}$ and the approximation induces an error of $\frac{1+\sqrt{2}}{2e^{\sqrt{2}\kappa t}} = 14.8\%$. By comparison, all the excluded high concentration end points have 10% completion time $t < 140 \text{ s}$.

S5 Nucleated dendritic growth

S5.1 Execution of the reaction graph

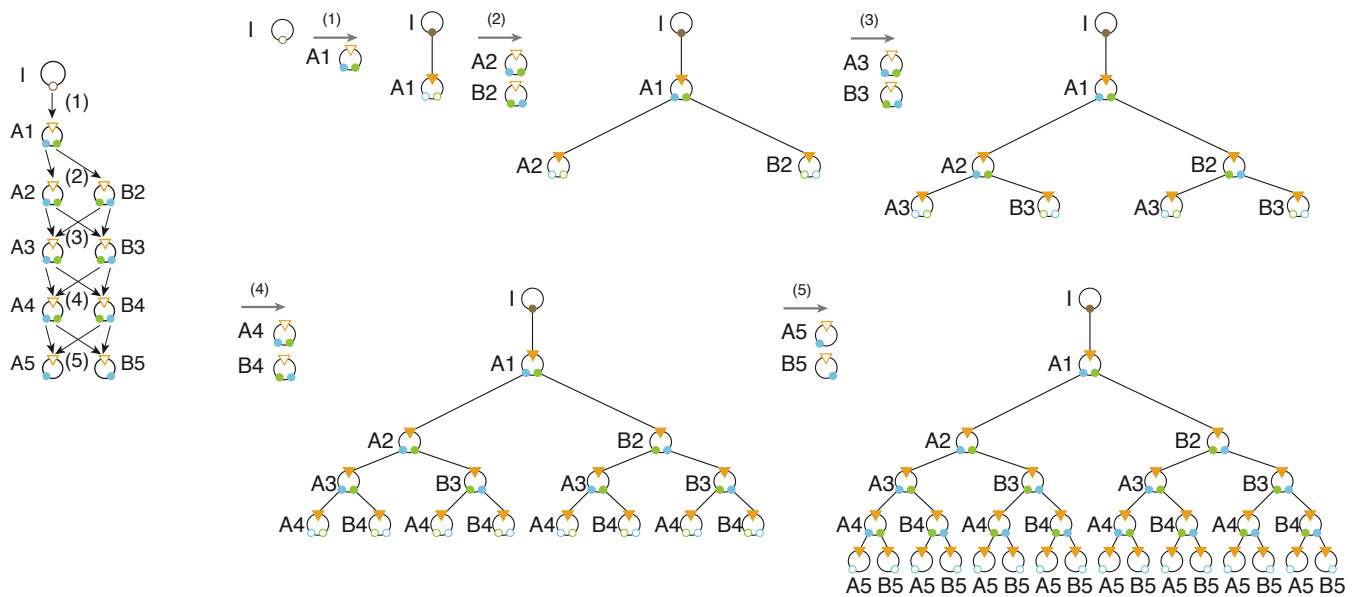


Figure S14. Execution of the reaction graph for the nucleated dendritic growth system.

Fig. S14 depicts the execution of the reaction graph of Fig. 4a. We omit a detailed description of the reaction graph execution, but note: (1) the multiple arrows entering the same input port depict parallel processes on separate copies of the nodal species, (2) the parallel processes are not synchronized and hence it is possible, for example, that after A1 assembles with A2, the assembly of A2 with A3 occurs before the assembly of A1 with B2.

S5.2 Detailed secondary structure mechanism

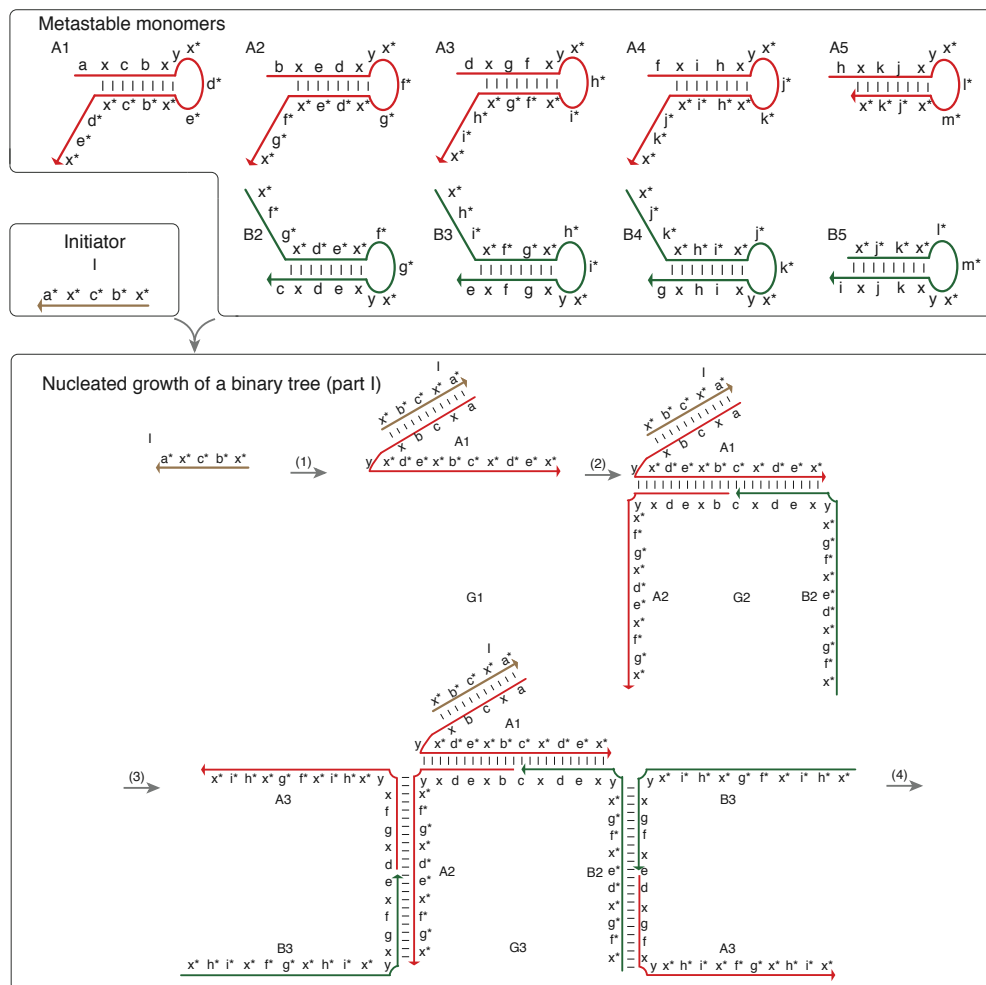


Figure S15. Reaction schematic of the nucleated dendritic growth system (part I). Step-by-step reaction schematic of the nucleated dendritic growth system, as described in Fig. 4. The lengths of segments x , x^* , and y are 2 nt; the lengths of the other segments are 7 nt. The figure continues in Fig. S16.

Fig. S15 and Fig. S16 present the detailed reaction schematic of the nucleated dendritic growth system described in Fig. 4. In the absence of the initiator I , hairpin monomers co-exist metastably. The initiator I triggers the system to self-assemble into a binary tree of a prescribed size.

- Step 1: the toehold a^* of the initiator I nucleates at the toehold a of hairpin $A1$, resulting in the opening of $A1$ and the formation of the first generation dendrimer, $G1$.
- Step 2: $A1$, with b^* and c^* newly exposed, opens hairpins $A2$ and $B2$, producing the second generation dendrimer, $G2$. Note that now $A2$ and $B2$ reveal single-stranded tails of identical sequences.
- Step 3: $A2$ and $B2$, with d^* and e^* newly exposed, open hairpins $A3$ and $B3$, producing $G3$.
- Step 4: each copy of $A3$ and $B3$, with its newly exposed f^* and g^* , opens hairpins $A4$ and $B4$, producing $G4$.
- Step 5: each copy of $A4$ and $B4$, with its newly exposed h^* and i^* , opens hairpins $A5$ and $B5$, producing $G5$.

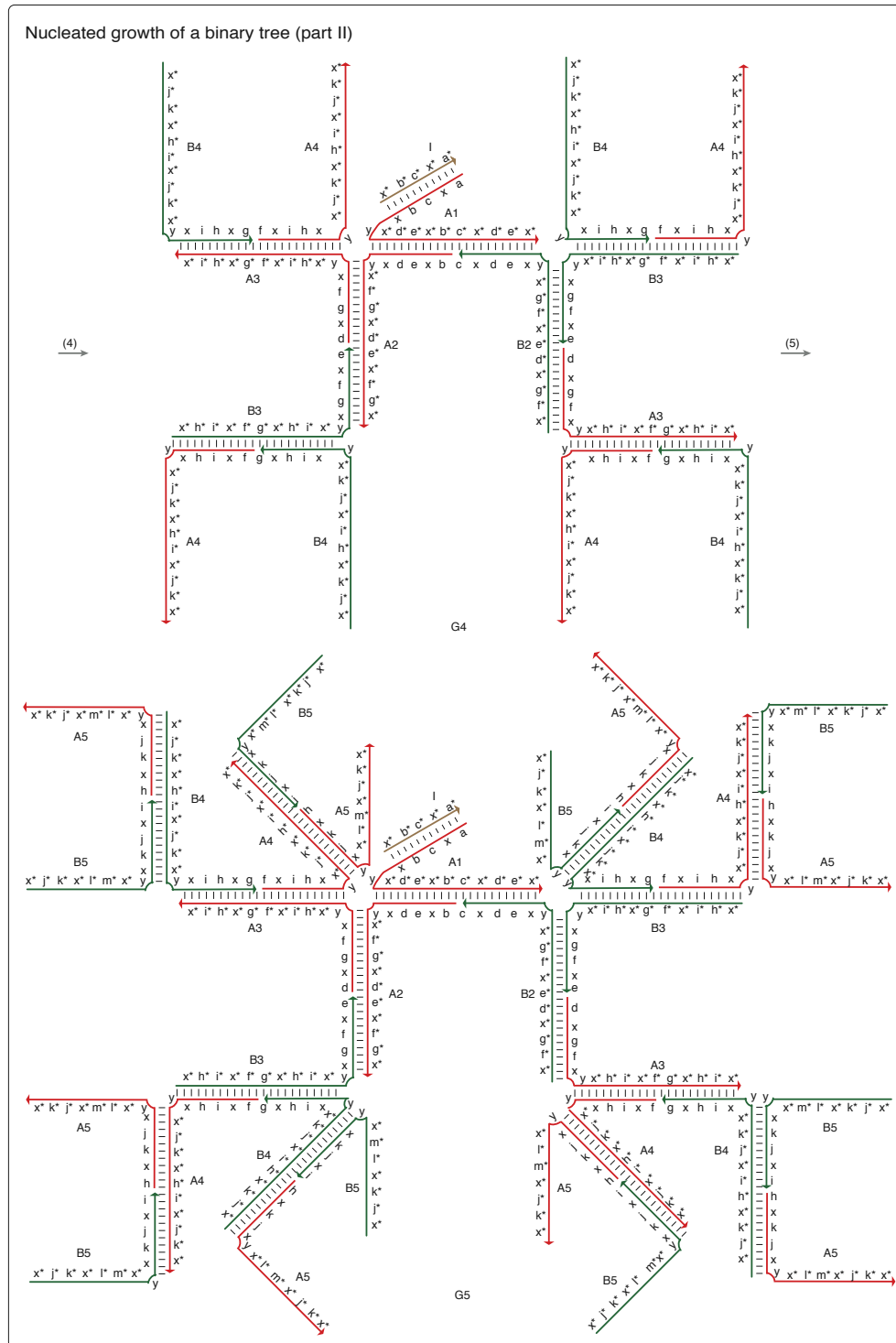


Figure S16. Reaction schematic of the nucleated dendritic growth system (part II). Step-by-step reaction schematic of the nucleated dendritic growth system, as described in Fig. 4. The figure continues from Fig. S15.

S5.3 Quantitative amplification gel

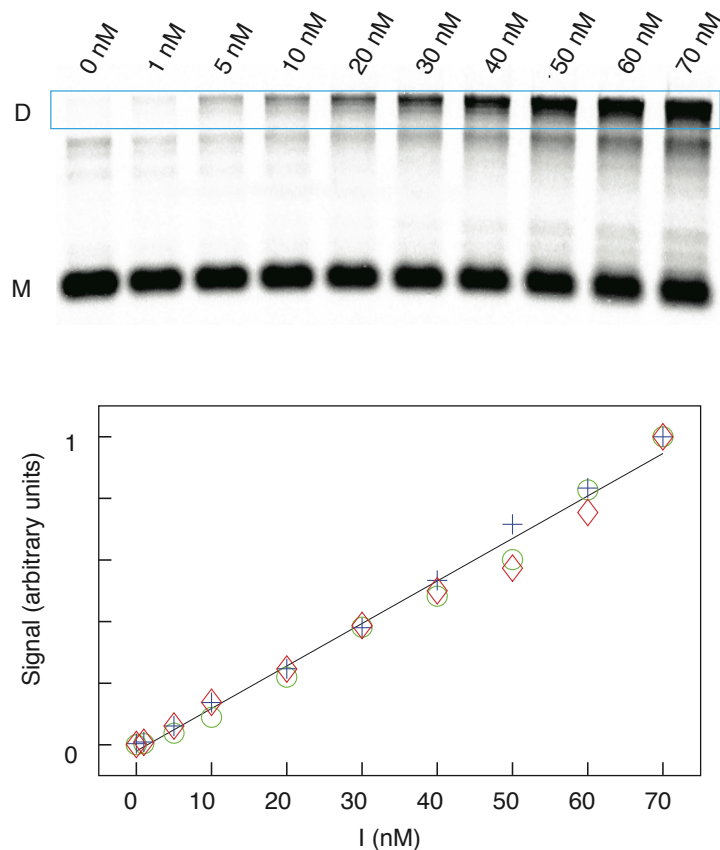


Figure S17. Agarose gel electrophoresis demonstrating quantitative amplification. Top: different concentrations of initiator incubated with all hairpin species (A1, A2, B2, 91 nM; the concentration doubles for each subsequent generation of hairpins). The gel measures fluorescence emission from Cy5, which is used to label hairpin A1. D denotes dendrimers; M denotes monomers. Bottom: Linear fit between the fluorescence signal of the dominant reaction product versus the concentration of initiator. Data from three independent experiments are denoted respectively by blue crosses, red diamonds, and green circles. Each set of data is normalized by the signal obtained at 70 nM initiator concentration.

Fig. S17 demonstrates that the concentration of dendrimer depends linearly on the concentration of the initiator in the system.

S5.4 AFM image analysis

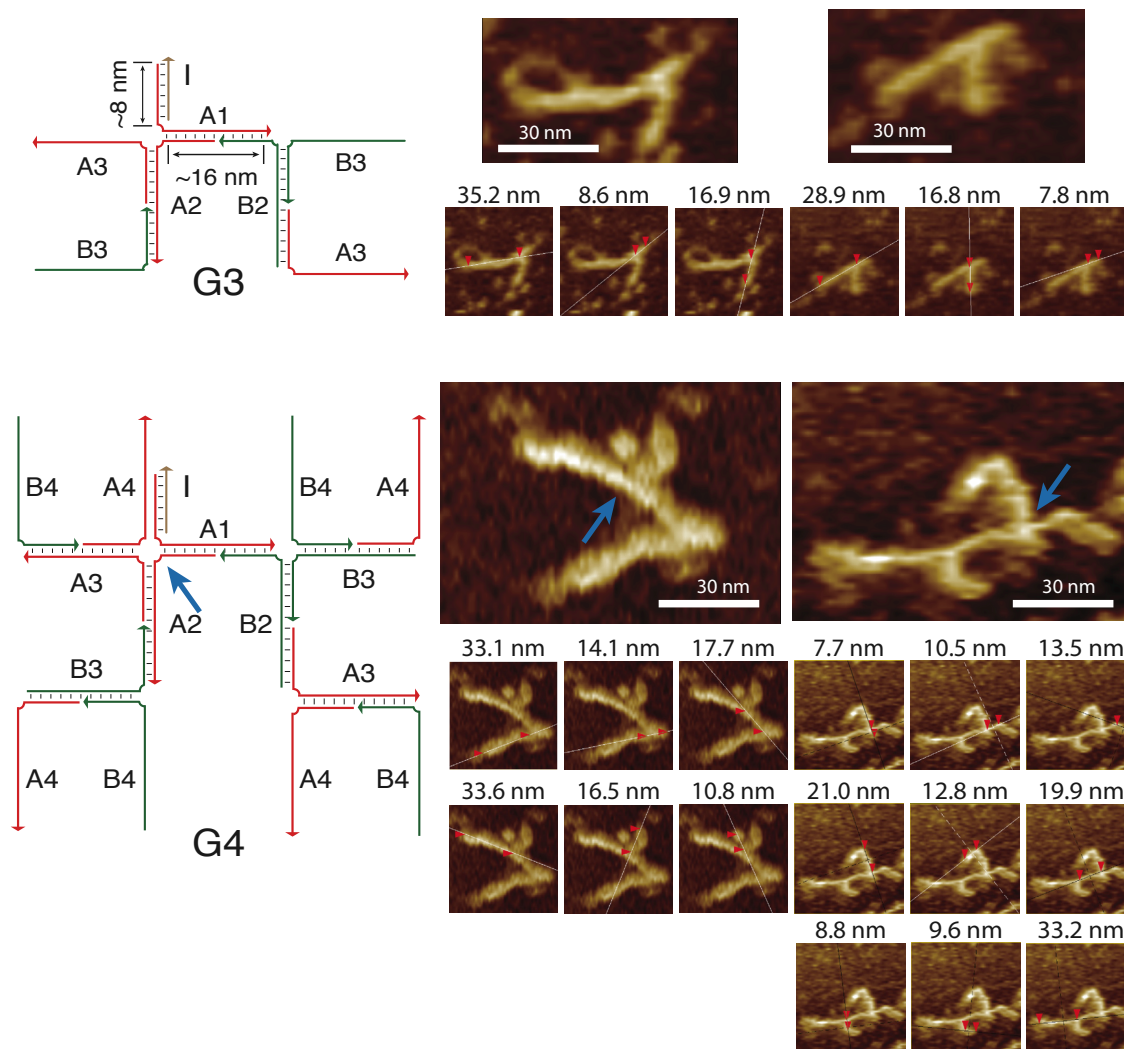


Figure S18. AFM measurements of the G3/G4 dendrimers. The small images are screenshots of the measurement section files. The distance between the two red arrowheads is listed above the image. The blue arrows point to the 4-arm junction in both the schematic and the images and help to relate the images to the schematic.

Using a B-DNA model where one helical turn contains 10.5 base pairs and measures 3.4 nm, we calculate the expected arm length for the duplex formed by A1 and I to be $25 / 10.5 \times 3.4 \text{ nm} = 8.1 \text{ nm}$ and the approximate length of all the other duplex segments to be $50 / 10.5 \times 3.4 \text{ nm} = 16.2 \text{ nm}$. Fig. S18 shows the image analysis for G3 and G4 dendrimers; Fig. S19 shows the image analysis for G5 dendrimers. The measured lengths of the arms are roughly consistent with the calculated lengths. Fig. S20 shows a large field-of-view AFM image of the G5 system. Note that in most AFM images, only the duplex portions of the dendrimer are visible.

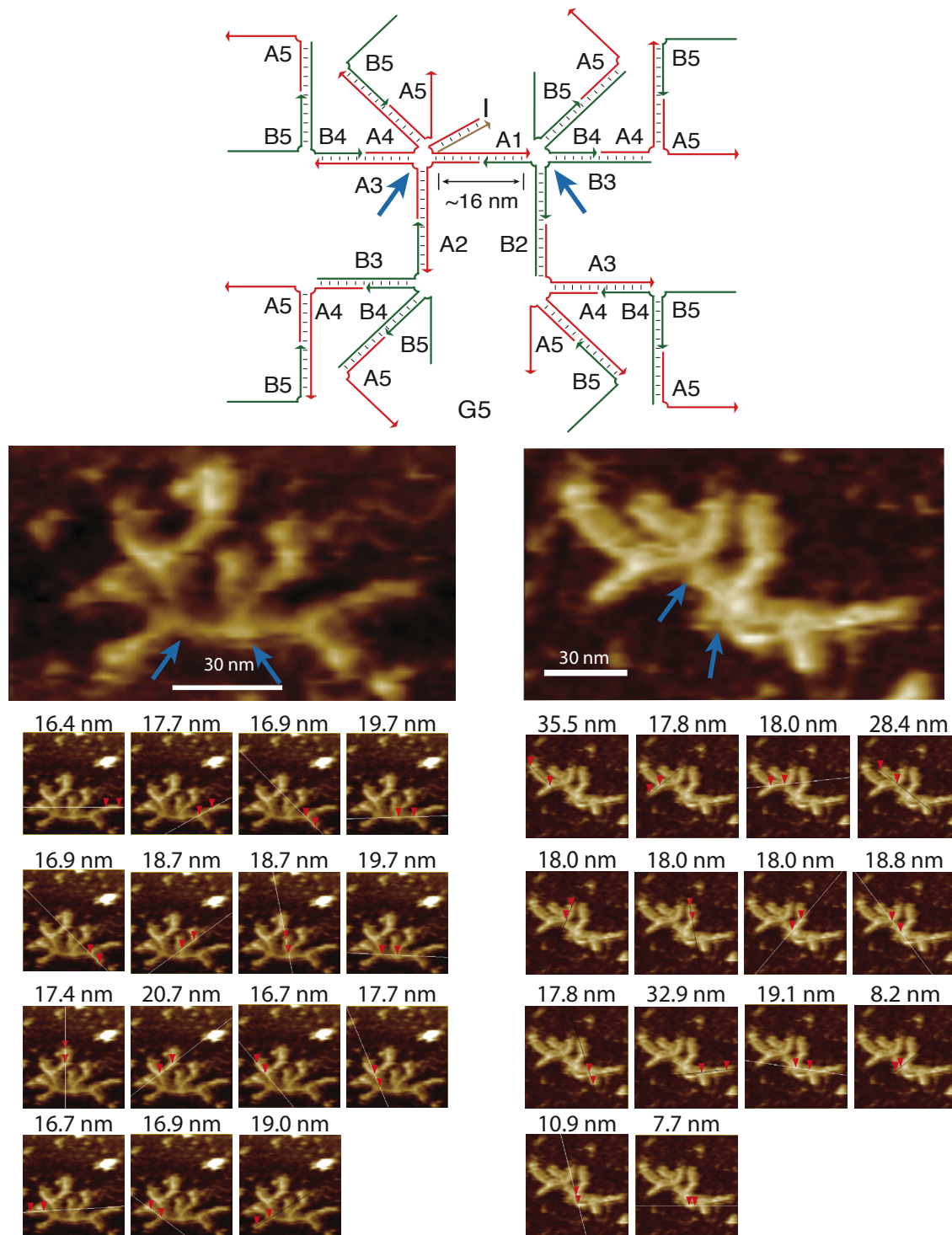


Figure S19. AFM measurements of the G5 dendrimers. The distance between the two red arrowheads is listed above the image. The blue arrows point to the 5-arm/4-arm junctions in both the schematic and the images and help to relate the images to the schematic. Note that the duplex A-I is not visible for the image in the left panel, likely due to damage during sample preparation or AFM scanning.

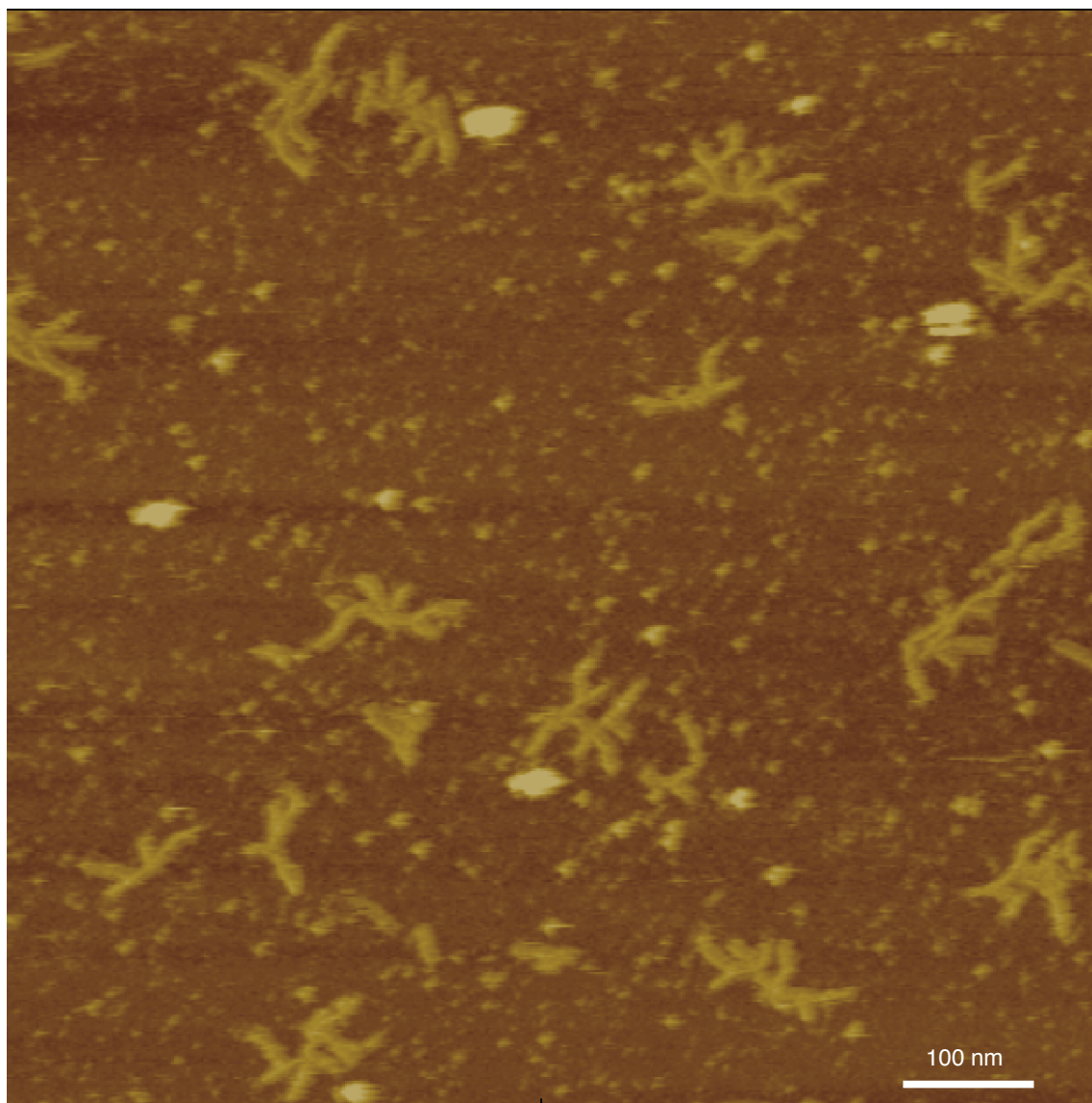


Figure S20. Large-field-of-view AFM image of the G5 dendrimer system.

S6 Autonomous locomotion

S6.1 Execution of the reaction graph

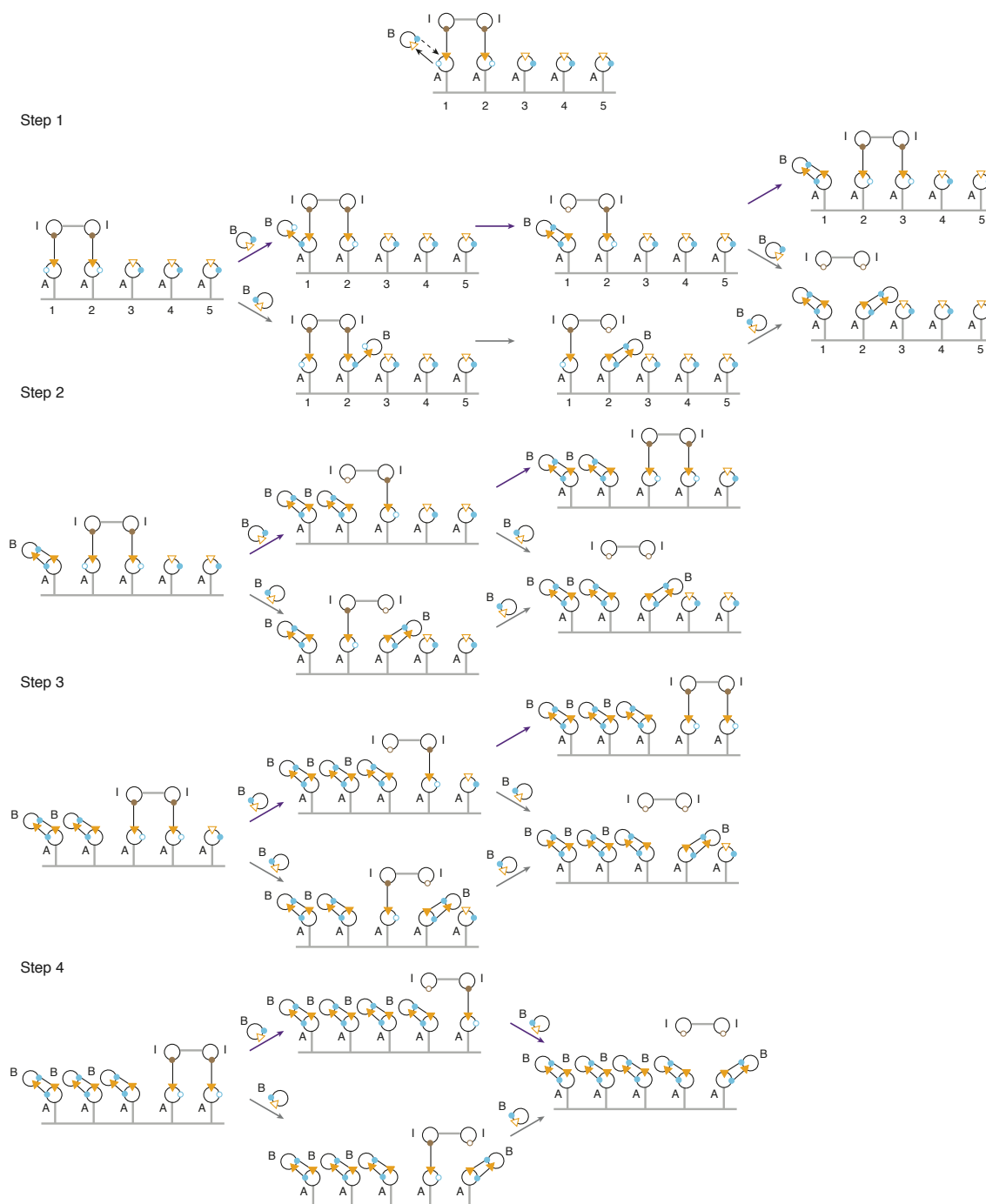


Figure S21. Execution of the reaction graph for the autonomous walker system of Fig. 5. Reaction steps corresponding to the processive sub-population of walkers are shown in purple. In the initial conditions prior to Step 1, the input ports of the A nodes at sites 1 and 2 are bound to the output ports of the I nodes on the bipedal walker. Execution begins with an assembly reaction between the accessible output port on either of these A nodes and the accessible input port on B. In the top route of Step 1, B assembles with A at site 1, resulting in the disassembly of the trailing I from A, which is then free to assemble with A at site 3, moving the walker one step down the track and bringing the system to Step 2. Alternatively, a B node could bind to A at site 2 prior to the assembly of I with A at site 3, resulting in the disassembly of the walker from the track. The walker could then diffuse through the bulk solution and re-attach to the same track or another track at any A monomer that has not yet been occupied. In the bottom route of Step 1, node B assembles with node A at site 2, resulting in the disassembly of the leading I from A. Due to geometric constraints (inextensible walker torso and rigid track backbone), the walker cannot attach to site 1 and site 3 simultaneously and hence will eventually detach from the track when a B node assembles with A at site 1. Similarly, in Step 2 and Step 3, processive stepping occurs stochastically for a sub-population of walkers. In Step 4, the walker will disassemble from track.

S6.3 Detailed secondary structure mechanism

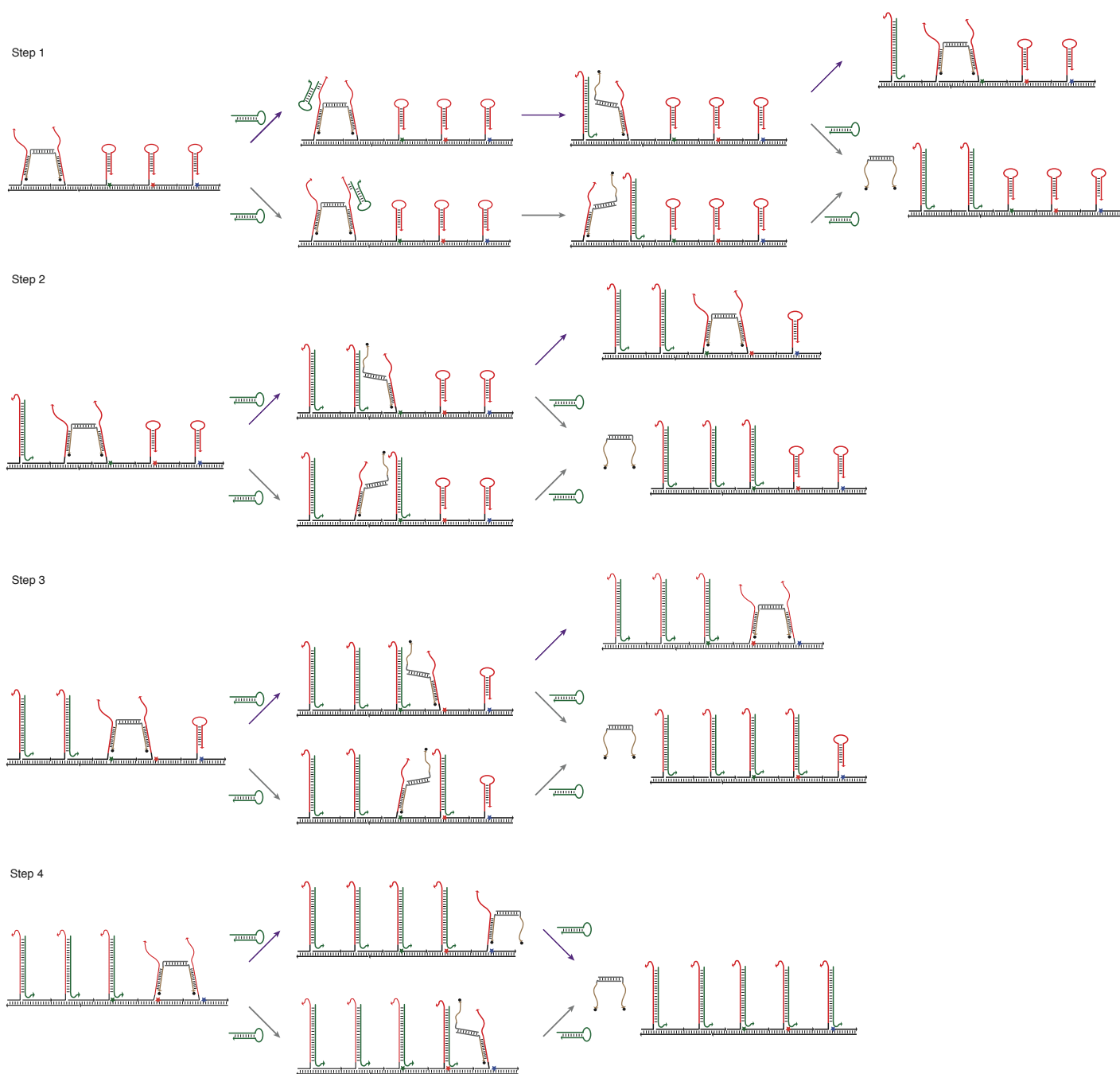


Figure S23. Step-by-step secondary structure schematic for the autonomous walker system of Fig. 5. Reaction arrows corresponding to the processive sub-population of walkers are shown in purple.

Fig. S23 depicts the step-by-step secondary structure schematic corresponding to the reaction graph of Fig. S21. A more detailed view of Step 1 is shown in Fig. S24.

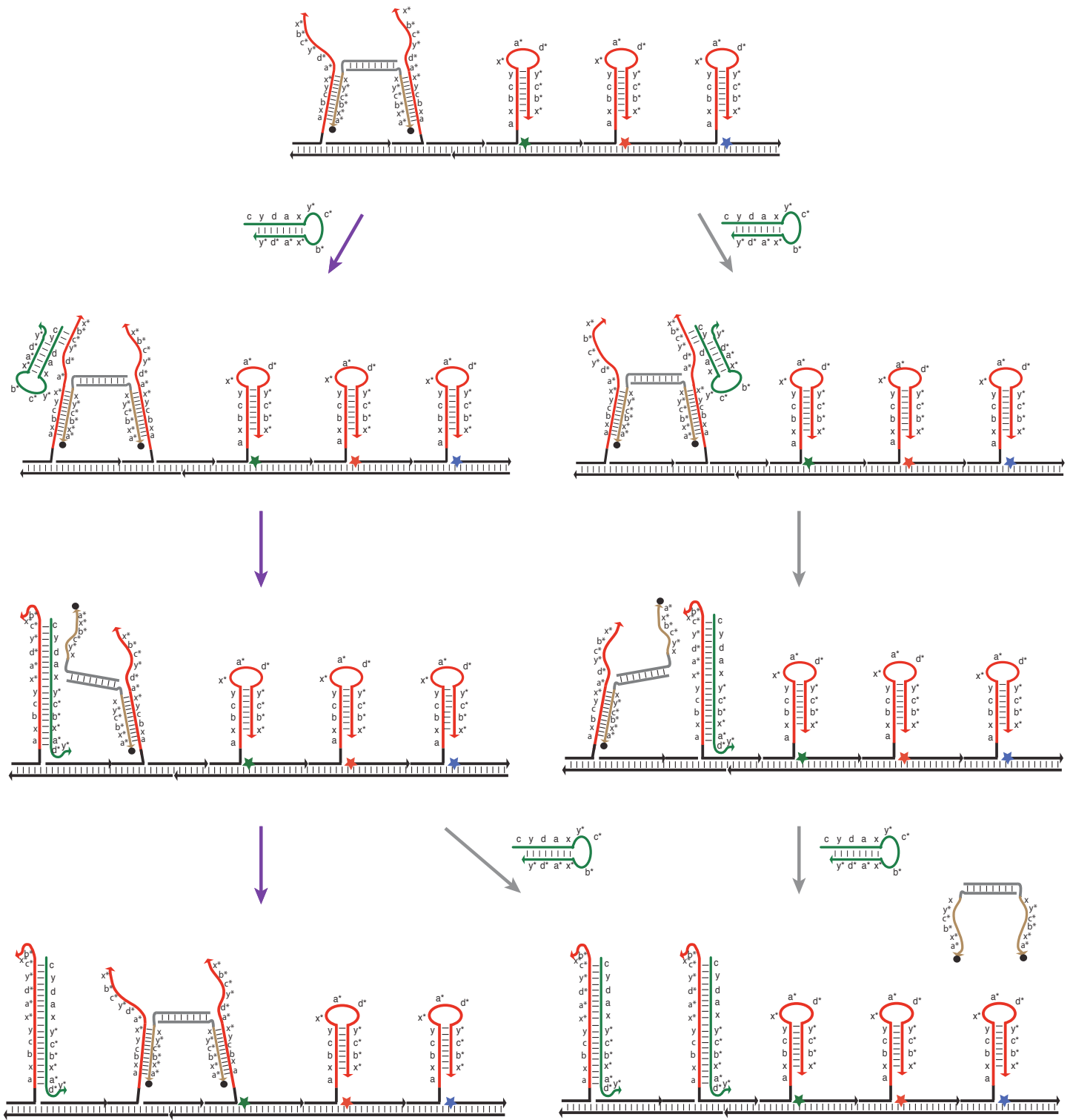


Figure S24. Detailed secondary structure schematic for Step 1 of Fig. S23. Reaction arrows corresponding to the processive sub-population of walkers are shown in purple.

S6.4 Assembly of the walker system

The walker system was assembled in four steps (Fig. S25a).

- Step 0. The walker (W) was assembled by annealing strands W1-BHQ1 and W2-BHQ1 as follows: heat the mixture at 95 °C for 5 minutes and slowly cool to room temperature over the course of 4 hours.
- Step 1. Hairpins S1 and S4 were mixed with track strands S2, S3, and S5, then annealed to produce Track 1 (T1) as follows: heat the system at 95 °C for 5 minutes; slowly cool to room temperature over the course of 4 hours.
- Step 2. T1 and the pre-assembled walker (W) were incubated at room temperature for 2 hours to produce T1+W.
- Step 3. Hairpins S6, S9, and S11 were mixed with track strands S7, S8, S10, and S12, then annealed to produce Track 2 (T2) as follows: heat the system to 95 °C for 5 minutes; slowly cool to room temperature over the course of 4 hours. For the bipedal and monopedal landing control experiments (Fig. S32), the S7 track strand is replaced by S7truncated (see Fig. S40b) so that T1 and T2 remain disjoint.
- Step 4. T2 and T1+W were incubated at room temperature for 3 hours to produce the final system, T1+W+T2.

Native agarose gel electrophoresis demonstrates a band shifting pattern that confirms on a step-by-step basis the correct assembly of the walker system. (Fig. S25b).

S6.5 Characterization of the fuel system

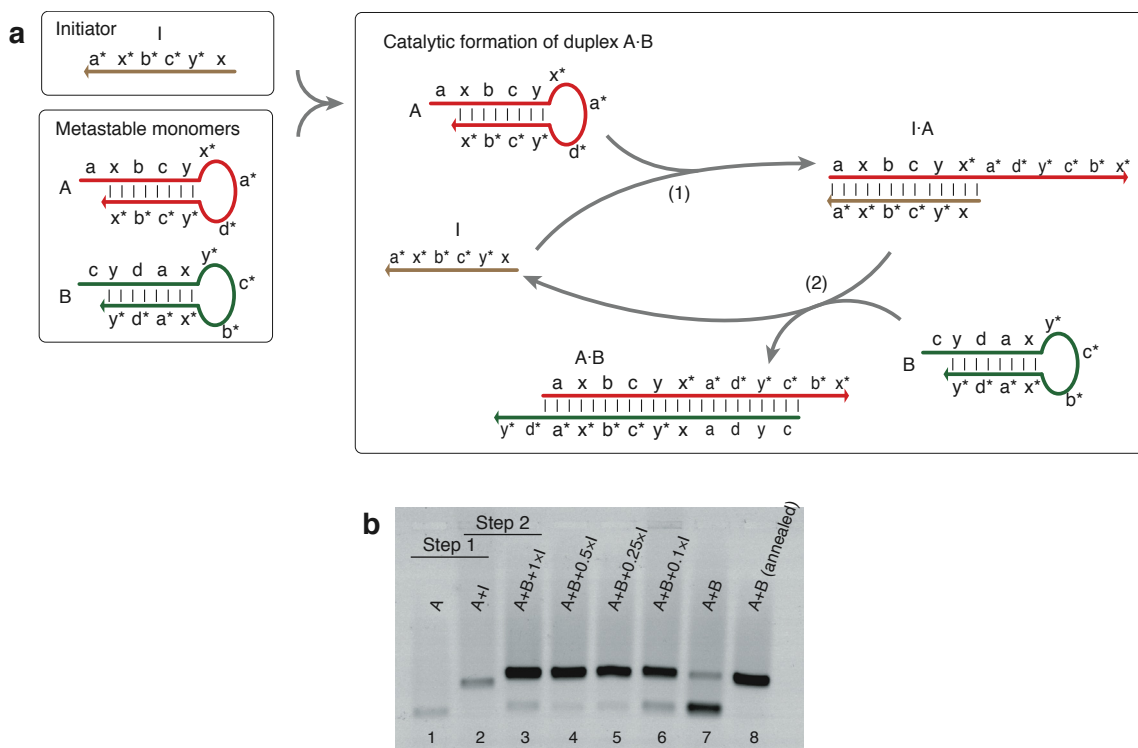


Figure S26. Fuel system for the walker system. **a**, Reaction schematic. Hairpins A and B co-exist metastably in the absence of catalyst I. Catalyst I catalyzes A and B to form duplex A·B. Step 1: the toehold a^* of I nucleates at the toehold a of A, resulting in the opening of the hairpin A and the formation of the product I·A. Step 2: I·A, with c^* newly exposed, opens hairpin B; B subsequently displaces I from A, producing waste product A·B. **b**, Agarose gel electrophoresis demonstrates catalytic formation of the DNA duplex. The hairpins were prepared in reaction buffer (4 mM $MgCl_2$, 15 mM KCl, and 10 mM Tris-HCl, pH = 8.0) using a snap-cooling procedure: heating at 90 °C for 5 minutes and cooling on ice for 1 minute. The hairpins were allowed to equilibrate at room temperature for 30 minutes before use. Lanes 1-3: A gel shifting assay validates each reaction step depicted in panel (a). Lanes 3-7: Effects of different concentrations of I (1×, 0.5×, 0.25×, 0.1×, and 0×) on the formation of A·B. Reactants were incubated at 1 μ M at room temperature for 2 hours. Lane 8: A·B annealed over 2.5 hours (1 μ M hairpin species heated at 95 °C for 5 minutes and cooled to room temperature over 2.5 hrs). Upon completion of the reaction, the samples were loaded with 5× SYBR Gold stain (Invitrogen) and 10% glycerol into a 2% native agarose gel, prepared with 1× LB buffer (Faster Better Media, LLC). The gel was run at 350 V for 10 minutes at room temperature and visualized using an FLA-5100 imaging system (Fuji Photo Film Co., Ltd.).

Fig. S26 describes the fuel system that powers the walker system. Here, hairpins A and B co-exist metastably in the absence of catalyst I. Catalyst I catalyzes A and B to form duplex A·B. Native gel electrophoresis (Fig. S26b) confirms that the hairpins assemble slowly in the absence of the initiator (Lane 7) and that the assembly is dramatically accelerated by the addition of initiator (Lane 3). Disassembly of the initiator enables catalytic turnover as indicated by the nearly complete consumption of hairpins even at sub-stoichiometric initiator concentrations (Lanes 4-6).

Catalyst recovery was further investigated using a fluorescence quenching experiment (Fig. S27). An initiator labeled with fluorophore FAM (6-carboxyfluorescein) is incubated with hairpin A. The hybridization of I with A results in the quenching of the FAM signal, presumably due to hybridization induced proximity of FAM to the guanine near the 5' end of hairpin A.⁵ Introduction of hairpin B releases I from A and hence leads to fluorescence signal recovery (Fig. S27a). The observed near-complete recovery of the fluorescence signal (after dilution correction) confirms the near-complete recovery of the catalyst (Fig. S27b).

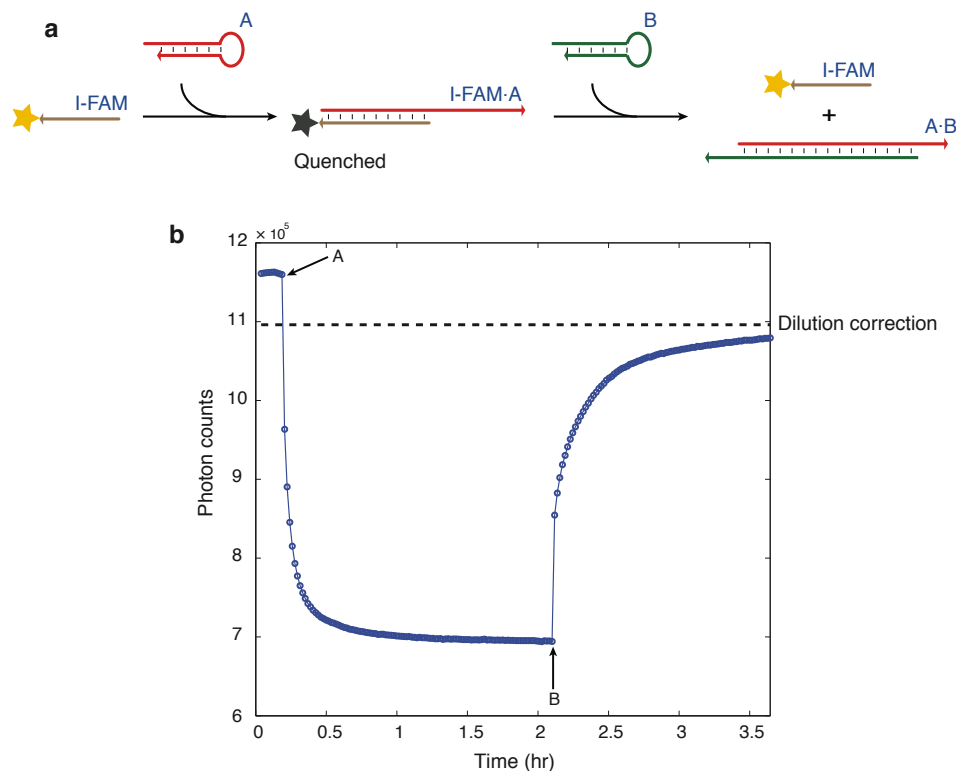


Figure S27. Fluorescence quenching experiment demonstrating catalyst recovery. **a**, Experimental design. **b**, Fluorescence data. The data were obtained using a fluorometer from Photon Technology International equipped with a temperature controller set at 21 °C. A 1.7 mL QS quartz cuvette (Hellma GmbH & Co. KG) was used. Excitation and emission wavelengths were set at 492 nm and 517 nm, respectively, with 4 nm bandwidths. Hairpin species A and B were each snap-cooled in the reaction buffer (4 mM MgCl₂, 15 mM KCl, and 10 mM Tris-HCl, pH = 8.0) by heating at 90 °C for 90 seconds and cooling at room temperature for 30 minutes before use. The reaction concentrations of I-FAM (I labeled with a fluorophore FAM) and A were 20 nM with B at 40 nM. After recording the baseline signal produced by the catalyst, I-FAM, hairpin A was introduced and resulted in fluorescence signal quenching. After the signal plateaued, hairpin B was introduced and near-complete signal recovery (after dilution correction) was observed.

S6.6 Raw data for the fluorescence quenching experiments

Fig. S28 and Fig. S29 present the raw data and curve fitting results for the fluorescence quenching experiments measuring the proximity of the quenchers (black dots) on the walker feet to the fluorophores (colored stars) decorating the track. In Fig. S28, the walker track is decorated with fluorophores JOE → TAMRA → FAM; in Fig. S29, the walker track is decorated with fluorophores TAMRA → JOE → FAM. For each dye ordering, six pairs of experiments were performed (each box contains data for one bipedal and one monopodal experiment that were performed simultaneously in separate cuvettes using the same instrument).

Since the walkers' motion is not synchronized, the time scale associated with the quenching of a given dye is characterized by approximating the minimum of the corresponding bulk fluorescence signal. To mitigate the effect of noise on estimating the location of the minimum, fitted double exponential curves (solid) were used to determine the time at which the minimum fluorescence (i.e., maximum quenching) was observed (dashed vertical line) for each fluorophore. For each curve fit, the data points of the initial baseline and those after the point of inflection are excluded (as depicted). The same time window was used for fitting all data for each pair of boxed experiments (i.e. for all six traces: 3 bipedal and 3 monopodal). All curve fits have an R^2 of 0.94 or better.

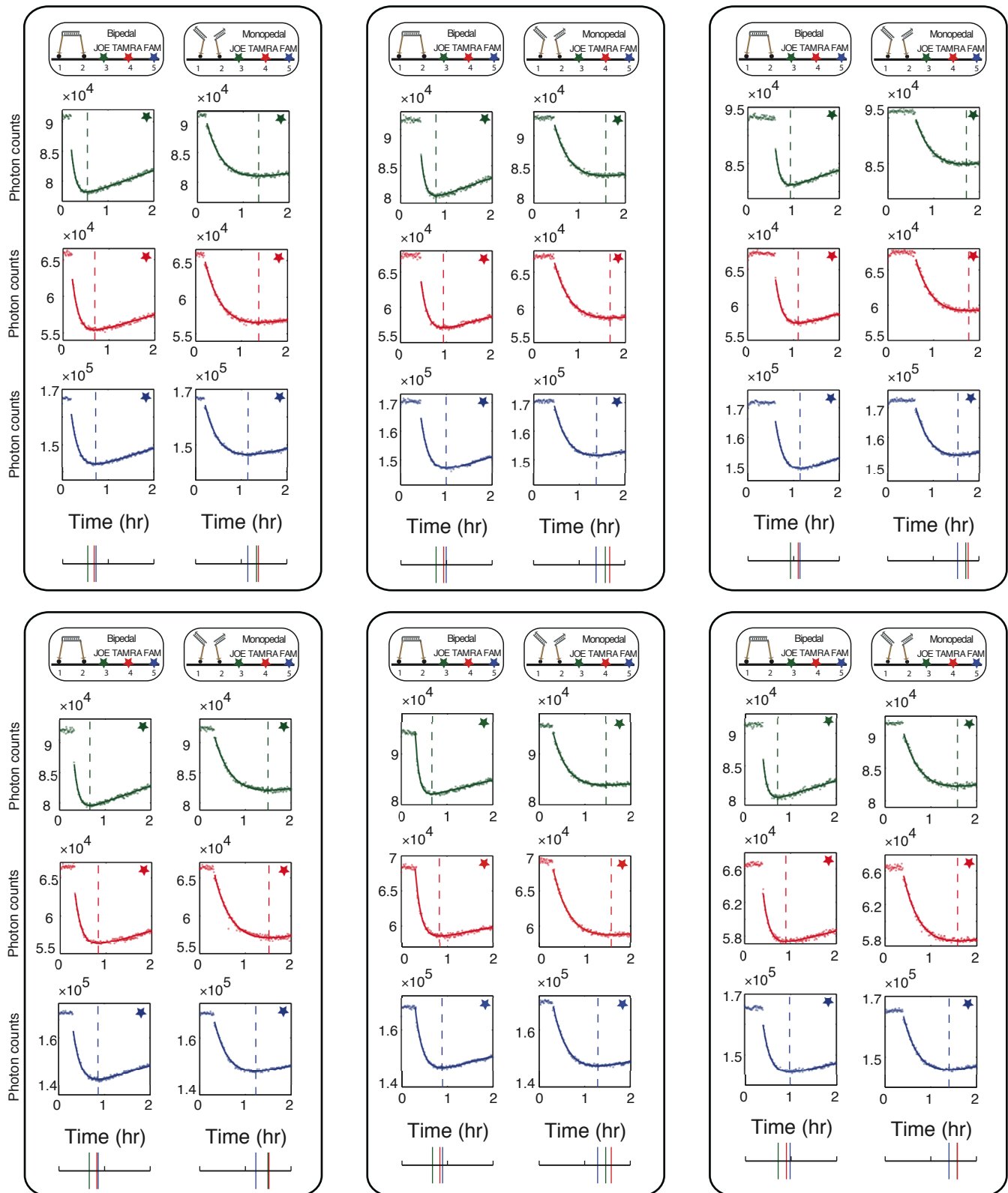


Figure S28. Fluorescence data for track with fluorophores JOE → TAMRA → FAM.

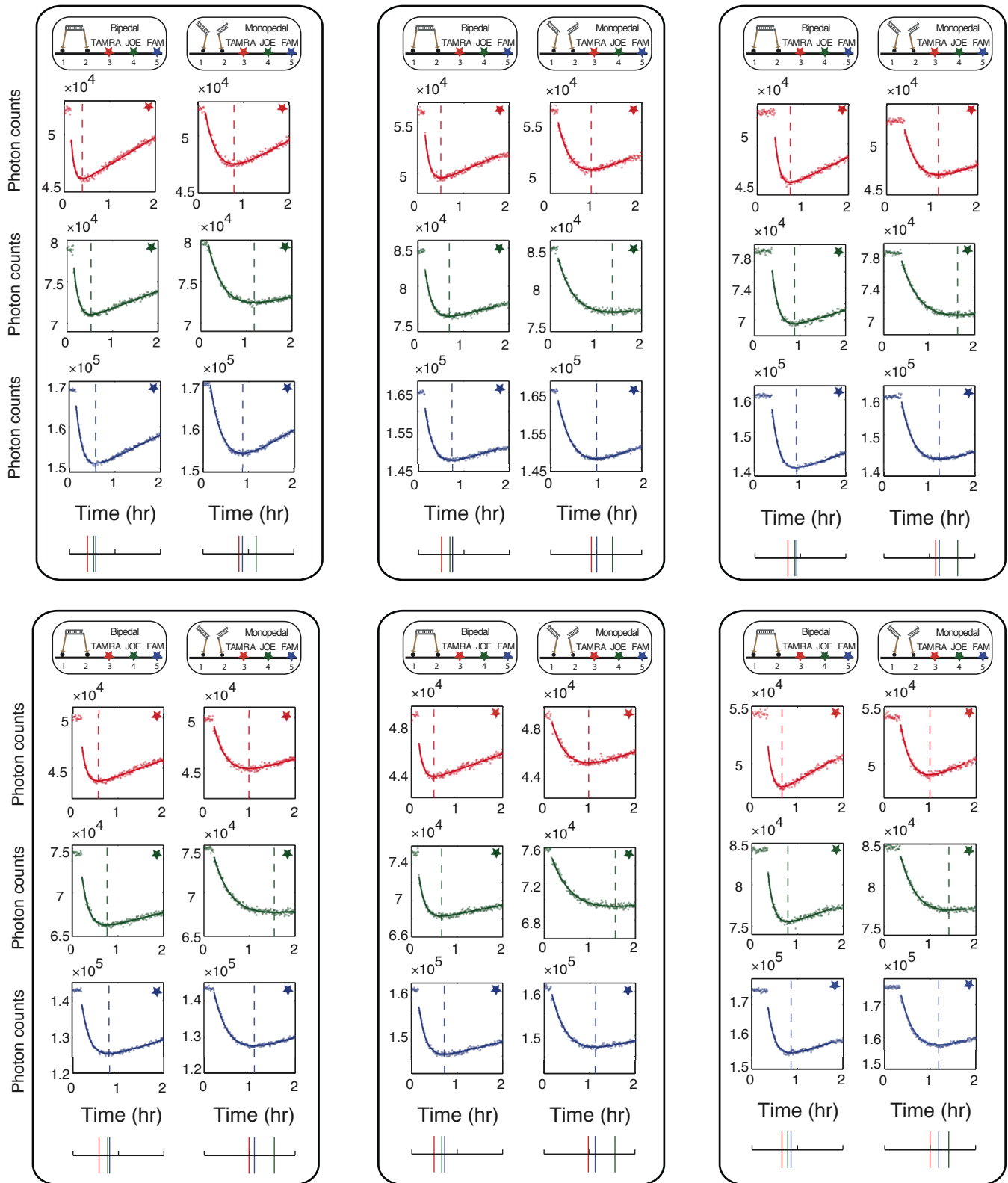


Figure S29. Fluorescence data for track with fluorophores TAMRA → JOE → FAM.

S6.7 Statistical analysis

For the bipedal walker experiment of Fig. 5c, the fluorophore ordering along the track is JOE \rightarrow TAMRA \rightarrow FAM. We wish to assess the statistical significance of the observation that the time differences between consecutive minima in the three quenching curves are positive (i.e., that $t_{\min}^{\text{TAMRA}} - t_{\min}^{\text{JOE}} > 0$ and $t_{\min}^{\text{FAM}} - t_{\min}^{\text{TAMRA}} > 0$). For the monopodal walker experiments of Fig. 5d with the same ordering of fluorophores along the track, we wish to test the statistical significance of the observations $t_{\min}^{\text{JOE}} - t_{\min}^{\text{FAM}} > 0$ and $t_{\min}^{\text{TAMRA}} - t_{\min}^{\text{JOE}} > 0$. Analogous questions apply to the bipedal and monopodal experiments where the fluorophores are instead ordered TAMRA \rightarrow JOE \rightarrow FAM along the track (data in Fig. 5f and Fig. S29).

For each time gap, we obtain six measurements (x_1, x_2, \dots, x_6 ; sample size $n = 6$) from independent experiments (Tables S1 and S2). To avoid making the assumption that the underlying distribution is normal, we employ the distribution-free sign test, which applies to any continuous distribution.⁶ Our null hypothesis is that the median of these measurements is zero ($H_0 : \tilde{\mu} = 0$); our alternative hypothesis is that the median is positive ($H_a : \tilde{\mu} > 0$). The test statistic, y , is the number of x_i 's that exceed 0; for all time gaps in Tables S1 and S2, $y = 6$ because all measured time differences are positive. Using a one-tailed sign test, the P -value is 0.0156 for all tests. Hence, the null hypothesis can be rejected for each time gap at significance level $\alpha = 0.0156$.

The above sign test analysis is preferred to the more familiar t -test analysis which requires the (unjustified) assumption of an underlying normal distribution. For purposes of comparison, we nonetheless include a t -test analysis (demonstrating that even smaller P -values are achieved under the assumption that the measurements are sampled from a normal distribution). In this case, the null hypothesis is that the mean of these measurements is zero ($H_0 : \mu = 0$); the alternative hypothesis is that the mean is positive ($H_a : \mu > 0$). The test statistic is $t = \mu / (s / \sqrt{n})$, where s is the computed standard deviation of the measurements.⁶ For a one-tailed t -test (with five degrees of freedom; $n - 1 = 5$), the P -values for all time gaps are shown in Tables S1 and S2. In each case, the P -value is smaller than the one for the corresponding sign test. Hence, the null hypotheses can be rejected with an even more stringent significance level α using the t -test.

Bipedal	x_1	x_2	x_3	x_4	x_5	x_6	Median ($\tilde{\mu}$)	Sign stat (y)	P -value	Mean (μ)	Std Dev (s)	t -stat	P -value
JOE \rightarrow TMR (sec)	515.5	588.3	621.8	590.1	669.2	658.5	606.0	6	0.0156	607.2	56.1	26.5	0.0000
TMR \rightarrow FAM (sec)	143.0	211.5	135.2	103.3	66.0	287.1	139.1	6	0.0156	157.7	79.7	4.8	0.0024
Monopodal	x_1	x_2	x_3	x_4	x_5	x_6	Median ($\tilde{\mu}$)	Sign stat (y)	P -value	Mean (μ)	Std Dev (s)	t -stat	P -value
FAM \rightarrow JOE (sec)	696.8	730.6	659.1	957.9	636.0	656.4	678.0	6	0.0156	722.8	120.0	14.8	0.0000
JOE \rightarrow TMR (sec)	144.6	337.0	184.8	74.3	443.6	3.4	164.7	6	0.0156	198.0	164.8	2.9	0.0169

Table S1. Measured time differences between minima and statistical analysis for six experiments with bipedal or monopodal walkers on the track with fluorophore ordering: JOE \rightarrow TAMRA \rightarrow FAM. For raw data see Fig. S28.

Bipedal	x_1	x_2	x_3	x_4	x_5	x_6	Median ($\tilde{\mu}$)	Sign stat (y)	P -value	Mean (μ)	Std Dev (s)	t -stat	P -value
TMR \rightarrow JOE (sec)	471.3	658.9	553.5	691.7	615.6	462.6	584.6	6	0.0156	575.6	96.1	14.7	0.0000
JOE \rightarrow FAM (sec)	178.1	216.2	144.0	143.1	215.8	245.6	197.0	6	0.0156	190.5	42.2	11.1	0.0001
Monopodal	x_1	x_2	x_3	x_4	x_5	x_6	Median ($\tilde{\mu}$)	Sign stat (y)	P -value	Mean (μ)	Std Dev (s)	t -stat	P -value
TMR \rightarrow FAM (sec)	286.4	427.5	284.1	428.0	542.0	692.2	427.8	6	0.0156	443.4	156.3	6.9	0.0005
FAM \rightarrow JOE (sec)	1092.4	1250.6	1430.4	1573.8	1575.1	799.0	1340.5	6	0.0156	1286.9	304.4	10.4	0.0001

Table S2. Measured time differences between minima and statistical analysis for six experiments with bipedal or monopodal walkers on the track with fluorophore ordering: TAMRA \rightarrow JOE \rightarrow FAM. For raw data see Fig. S29.

S6.8 Comparison of walker time scales

Figs S30 and S31 overlay the fitted curves from the six independent bipedal and monopedal walker experiments of Figs S28 and S29. To enable comparison in a single plot, all data is normalized: unity corresponds to the final baseline fluorescence value before adding hairpin B and zero corresponds to the minimum of the fitted curve. The time axis is translated so that $t = 0$ corresponds to the time of the final baseline data point before adding hairpin B. An upper bound on the variability in the time required to add hairpin B and mix the sample in each experiment is approximately 30 secs, representing the uncertainty in comparing curve fits from different experiments along the same time axis.

The variability in the traces for each fluorophore is higher in Fig. S31 (TAMRA \rightarrow JOE \rightarrow FAM) than in Fig. S30 (JOE \rightarrow TAMRA \rightarrow FAM). The conclusion drawn from this data, that the time scale to visit any one site with the monopedal walker is longer than the time scale to visit all three sites with the bipedal walker, follows from either data set.

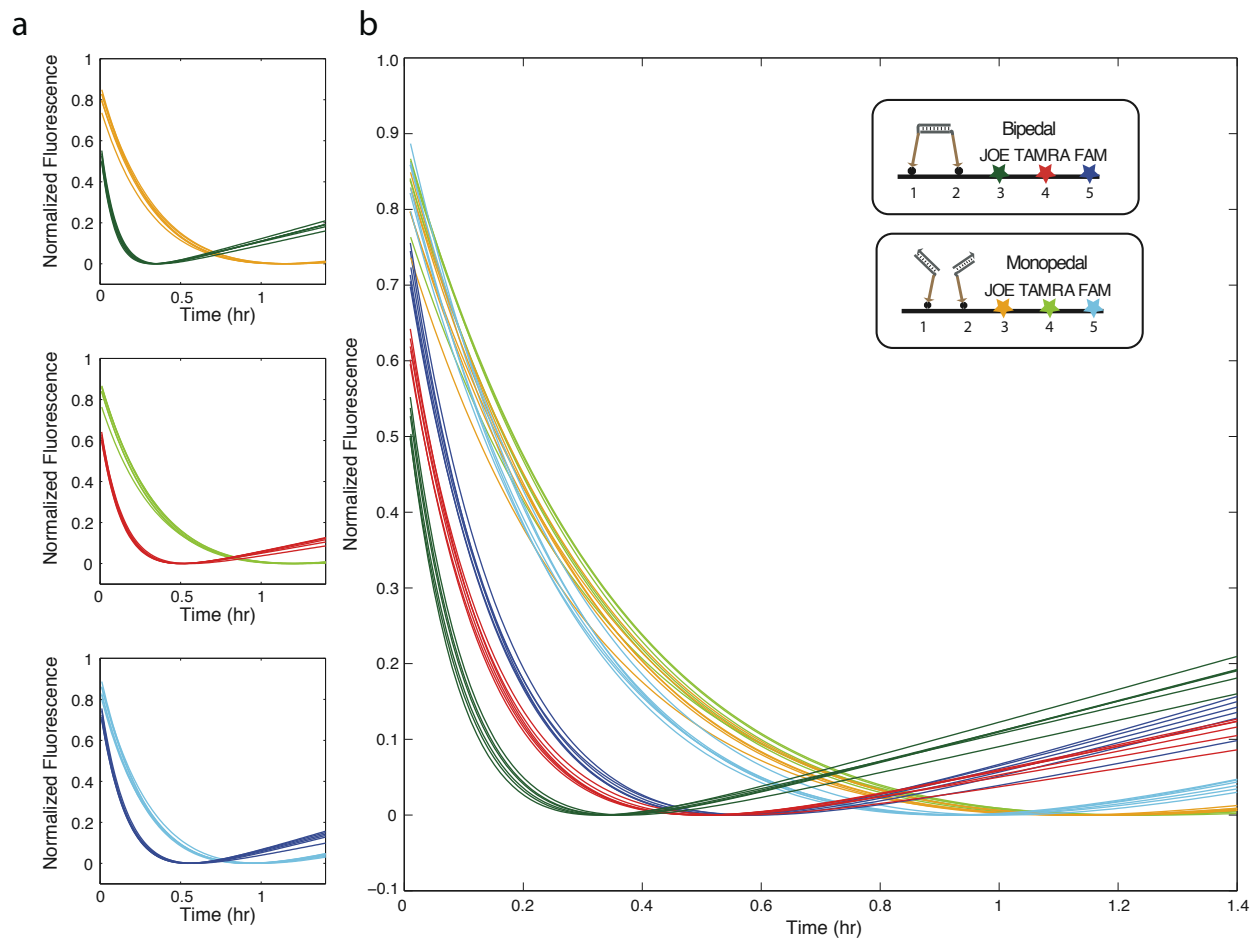


Figure S30. Comparison of time scales for bipedal and monopedal walkers using normalized fitted curves from the raw fluorescence data of Fig. S28 with track labeled JOE \rightarrow TAMRA \rightarrow FAM. **a**, For each fluorophore, 12 traces (six for each walker type) are plotted together, demonstrating that the bipedal walker visits each anchorage on a faster time scale than the monopedal walker. **b**, All 36 traces (18 per walker type) are plotted together to demonstrate that the time scale for the monopedal walker to visit any one of the three anchorages is longer than the time scale of the bipedal walker to visit all three anchorages.

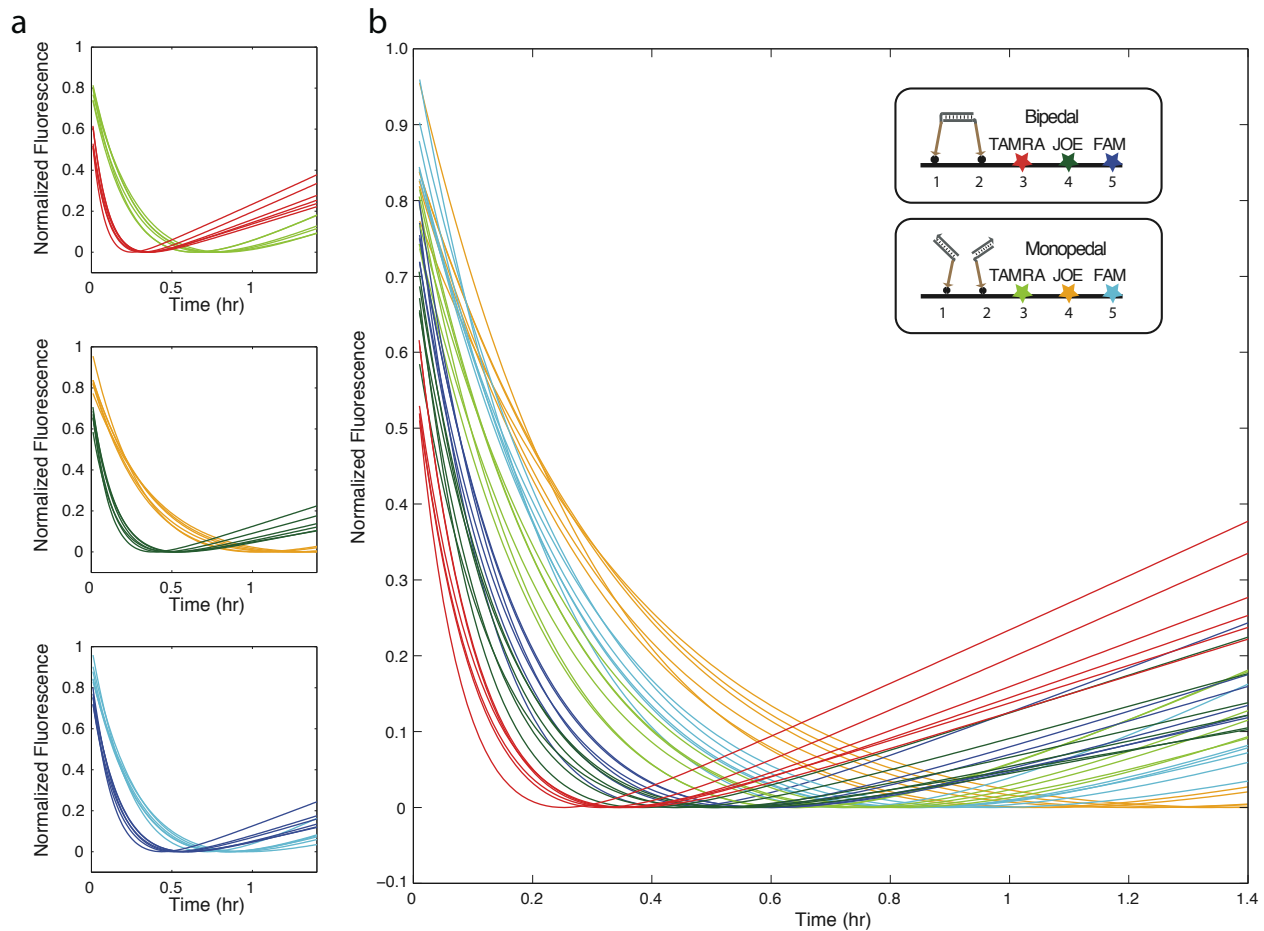


Figure S31. Comparison of time scales for bipedal and monopodal walkers using normalized fitted curves from the raw fluorescence data of Fig. S29 with track labeled TAMRA \rightarrow JOE \rightarrow FAM. **a**, For each fluorophore, 12 traces (six for each walker type) are plotted together, demonstrating that the bipedal walker visits each anchorage on a faster time scale than the monopodal walker. **b**, All 36 traces (18 per walker type) are plotted together to demonstrate that the time scale for the monopodal walker to visit any one of the three anchorages is longer than the time scale of the bipedal walker to visit all three anchorages.

S6.9 Control for walker landing effects

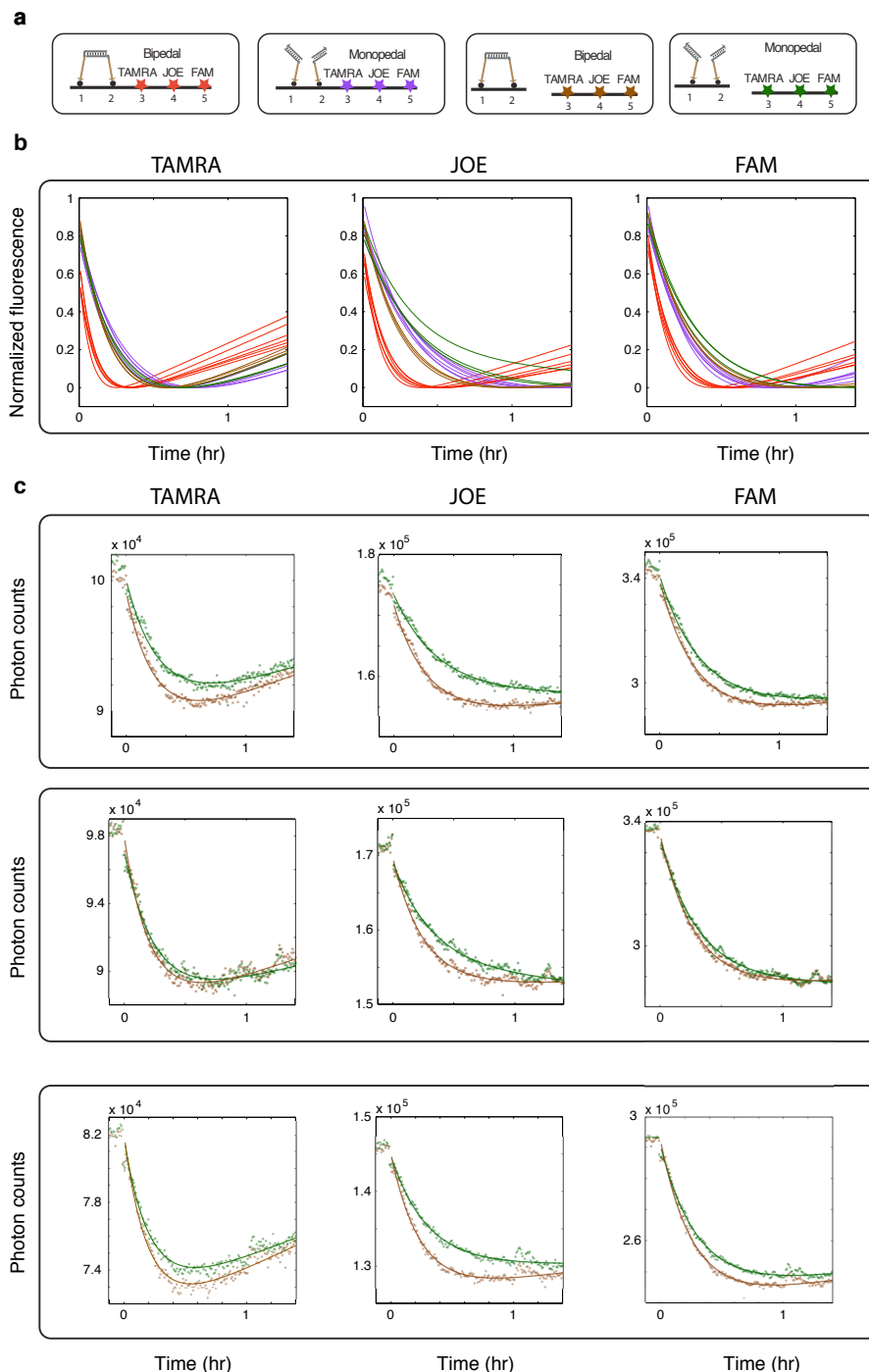


Figure S32. Comparison of time scales for bipedal and monopodal walkers on the full track and on a disjoint track that requires both walker types to diffuse through solution to land on the track (labeled TAMRA→JOE→FAM). **a**, These four types of experimental data are depicted with different colors. Red: Bipedal walker on the full track; purple: monopodal walker on the full track; brown: bipedal walker on the disjoint track; green: monopodal walker on the disjoint track. **b**, For each of the three sites (3, 4, 5), the time scale for the bipedal disjoint track walker (brown traces) is similar to those for the the monopodal full track walker (purple traces) and the monopodal disjoint track walker (green traces), and slower than the time scale for the bipedal walker on the full track (red traces). **c**, Raw fluorescence data and curve fits for the three pairs of bipedal and monopodal walker experiments on the disjoint track. The protocol for these landing experiments was the same as for the other walker fluorescence quenching experiments, with the exception that a disjoint track was pre-assembled as described in Sect. S6.4.

S7 Discussion

S7.1 Leakage and ligation

Commercially available synthetic single-stranded DNA oligos are impure and contain incorrectly synthesized strands.⁷ The presence of such erroneous strands contributes to the leakage of our systems. To improve strand purity and hence decrease system leakage, we use the following enzyme-based ligation method to synthesize the hairpin monomers: two constituent segments of a hairpin are synthesized and purified separately and ligated to produce the full hairpin (Fig. S33). For DNA sequence details, see Sect. S8. Significant reduction of system leakage in the ligation-based system is observed, as compared to the un-ligated system (data not shown).

We suggest that the observed error reduction may be attributed to the following two mechanisms. First, longer DNA strands contain more errors than shorter fragments, since the shorter fragments can be purified to a higher purity.⁷ As such, the two constituent segments contain fewer total errors than the full strand. Second, for T4 ligase mediated ligation of Ha and Hb, the successful ligation depends on the correct juxtaposition of the 5' end of fragment Hb with the 3' end of fragment Ha. This requirement provides an additional error reduction mechanism: DNA segments with errors in the regions adjacent to the nick position are not ligated successfully and are eliminated during the subsequent gel purification.

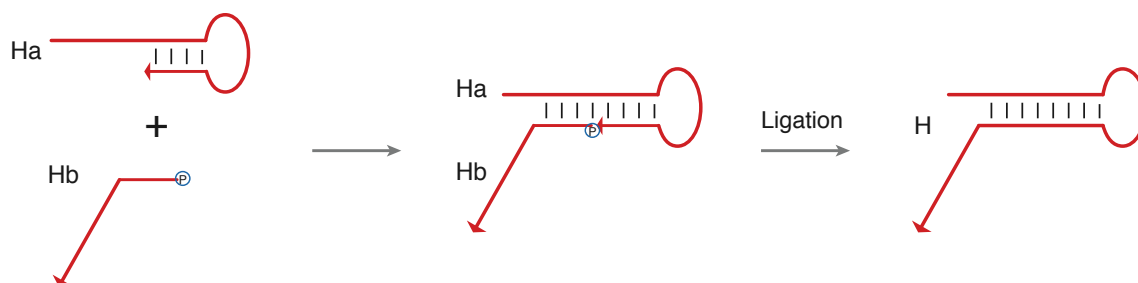


Figure S33. DNA hairpin synthesis by ligation. The circled P indicates a phosphate group, which is required for ligation by T4 ligase.

S7.2 Molecular compiler

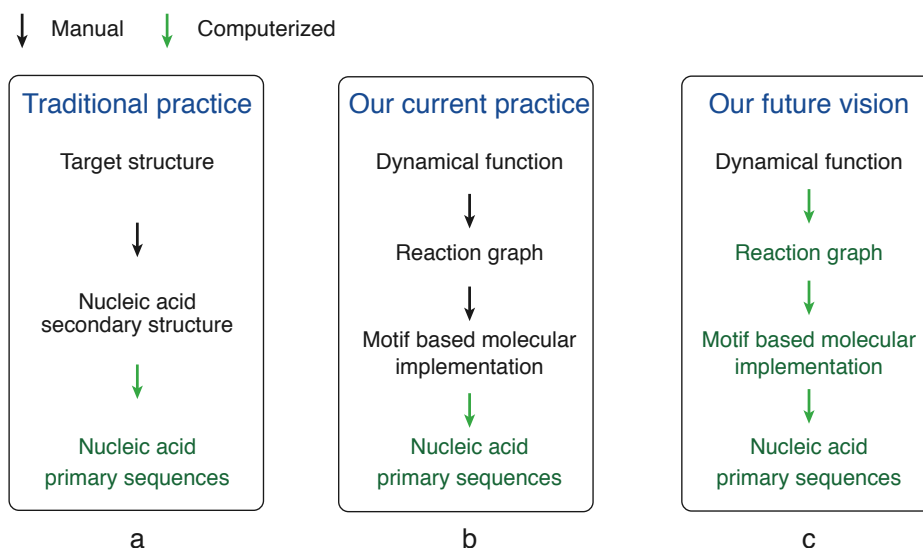


Figure S34. Schematic of the molecular compiler vision. **a**, Standard practice within the nucleic acid design community. **b**, Our current practice as described in Methods and in Sect. S3.1. **c**, Our future vision of an integrated compiler for biomolecular function.

Within the nucleic acid design community, it is common practice (Fig. S34a) to specify a design as a set of one or more static target secondary structures.⁸ The sequences of the constituent strands are then typically designed^{9–11} by optimizing an objective function that captures some combination of affinity and/or specificity for the target structures.¹²

By contrast, we design the dynamic function encoded in a self-assembly system by programming the reaction pathway of the system. The intended dynamic function is first specified using a reaction graph. The reaction graph is then implemented in terms of the present hairpin motif, and finally the molecular implementation is encoded in the primary sequences of a set of nucleic acid strands (Fig. S34b, also see Sect. S3.1 for details). As such, the standardized motif and the reaction graph provide layers of abstraction that bridge the description of the dynamic behavior of the system and the set of nucleic acid primary sequences, which implement the target behavior.

The translation of the target dynamic function to the reaction graph and the subsequent implementation of the reaction graph using the motif are performed manually in this paper. However, standardization of the reaction graph and the motif suggests the feasibility of automating the current manual process. Following this line of thinking, it may eventually be possible to create a compiler for biomolecular function (Fig. S34c). The compiler would take the desired dynamic function as input, translate it first to a reaction graph, then to a motif-based molecular implementation, and finally into nucleic acid sequences that encode the intended dynamic function.

S8 DNA sequences

The DNA sequences for the systems described in the paper are presented both as secondary structure schematics[†](Fig. S35, Fig. S37, Fig. S38, and Fig. S39) and as text sequences annotated with segment names.

Note:

- For each hairpin sequence X, the two segments that are ligated to produce X are indicated as Xa and Xb.
- Strand modifications are indicated as follows:

```
5' phosphorylation: /5Phos/;
3' Cy5: /3Cy5Sp/;
3' 6-carboxyfluorescein: /36FAM/;
5' 6-carboxyfluorescein: /56FAM/;
5' 6-carboxy-4',5'-dichloro-2',7'-dimethoxyfluorescein (NHS Ester): /5JOEN/;
5' tetrachlorofluorescein: /5TET/;
5' carboxytetramethylrhodamine (NHS Ester): /5TMRN/;
3' black hole quencher-1: /3BHQ_1/
```

S8.1 Catalytic 3-arm junction system

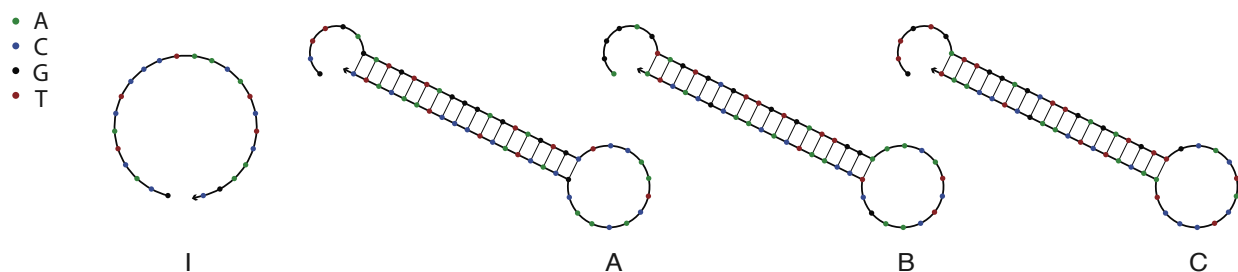


Figure S35. DNA sequences and secondary structures for the catalytic 3-arm junction system of Fig. 2.

The sequences are also listed below as text sequences annotated with segment names.

```
A: a-x-b-y-z*-c*-y*-b*-x*
GCTTGA-GATGTT-AGGGAG-TAGTGC-TCCAAT-CACAAC-GCACTA-CTCCCT-AACATC
```

```
Aa:
GCTTGAGATGTTAGG
```

```
Ab:
/5Phos/GAGTAGTGCTCCAATCACAACGCACTACTCCCTAACATC
```

```
B: b-y-c-z-x*-a*-z*-c*-y*
AGGGAG-TAGTGC-GTTGTG-ATTGGA-AACATC-TCAAGC-TCCAAT-CACAAC-GCACTA
```

```
Ba:
AGGGAGTAGTGCCTT
```

```
Bb:
/5Phos/GTGATTGGAACATCTCAAGCTCCAATCACAACGCACTA
```

```
C: c-z-a-x-y*-b*-x*-a*-z*
GTTGTG-ATTGGA-GCTTGA-GATGTT-GCACTA-CTCCCT-AACATC-TCAAGC-TCCAAT
```

```
Ca:
GTTGTGATTGGAGCT
```

```
Cb:
/5Phos/TGAGATGTTGCACTACTCCCTAACATCTCAAGCTCCAAT
```

```
I: y*-b*-x*-a*
GCACTA-CTCCCT-AACATC-TCAAGC
```

[†]The schematics are generated by the NUPACK server (www.nupack.org).

S8.2 Catalytic 4-arm junction system

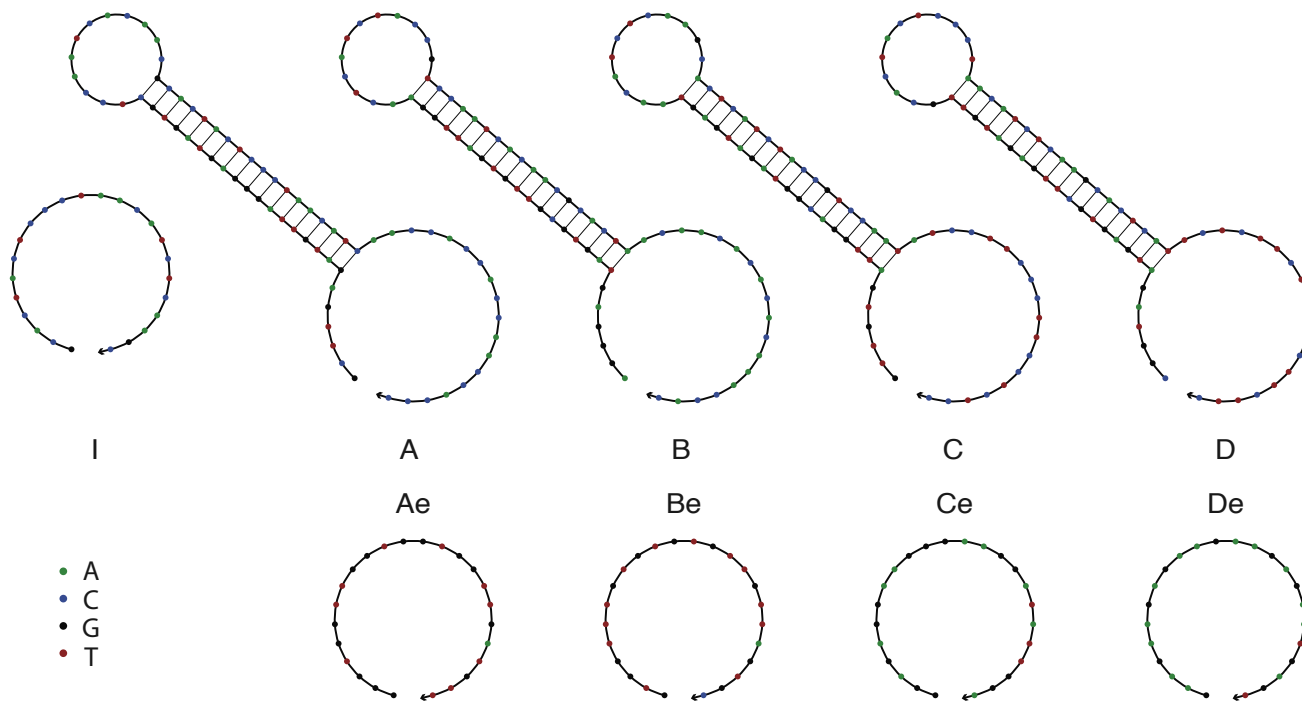


Figure S36. DNA sequences and secondary structures for the catalytic 4-arm junction system of Fig. S4.

The sequences are also listed below as text sequences annotated with segment names.

A: a-w-b-x-y*-c*-x*-b*-w*-q*
GCTTGA-GATGTT-AGGGAG-TAGTGC-TCCAAT-CACAAC-GCACTA-CTCCCT-AACATC-AACCACCACCAACCACC

Aa:
GCTTGAGATGTTAGGGAGTAGTGCTCCAATCACAACGCACTACTCC

Ab:
/5Phos/CTAACATCAACCACCACCAACCACC

B: b-x-c-y-z*-d*-y*-c*-x*-r*
AGGGAG-TAGTGC-GTTGTG-ATGGA-ACTCAT-CTACCG-TCCAAT-CACAAC-GCACTA-ACAACACACAAAACCAC

Ba:
AGGGAGTAGTGC GTTGTGATTGGA ACTCATCTACCGTCCAATCAC

Bb:
/5Phos/AACGCACTAACAACACACAAAACCAC

C: c-y-d-z-w*-a*-z*-d*-y*-s*
GTTGTG-ATGGA-CGGTAG-ATGAGT-AACATC-TCAAGC-ACTCAT-CTACCG-TCCAAT-ATCCTTCCCTTCTCTCC

Ca:
GTTGTGATGGACGGTAGATGAGTAACATCTCAAGCACTCATCTAC

Cb:
/5Phos/CGTCCAATATCCTTCCCTTCTCTCC

D: d-z-a-w-x*-b*-w*-a*-z*-t*
CGGTAG-ATGAGT-GCTTGA-GATGTT-GCACTA-CTCCCT-AACATC-TCAAGC-ACTCAT-TCTCTTCTTCTTCTTC

Da:
CGGTAGATGAGTGCTTGAGATGTGCACTACTCCCTAACATCTCAA

Db:
/5Phos/GCACTATTCTTCTTCTTCTTCTTC

I: x*-b*-w*-a*

GCACTA-CTCCCT-AACATC-TCAAGC

Ae: q-w

GGGTGGTTGGTGGTGGTT-GAIGTT

Be: r-x

GTGGTTTGTGTGTGTTGT-TAGTGC

Ce: s-y

GGAGAGGAAGGAAGGAT-ATTGGA

De: t-z

GAAGAAGAGAAGAAGAGA-ATGAGT

S8.3 Autocatalytic system

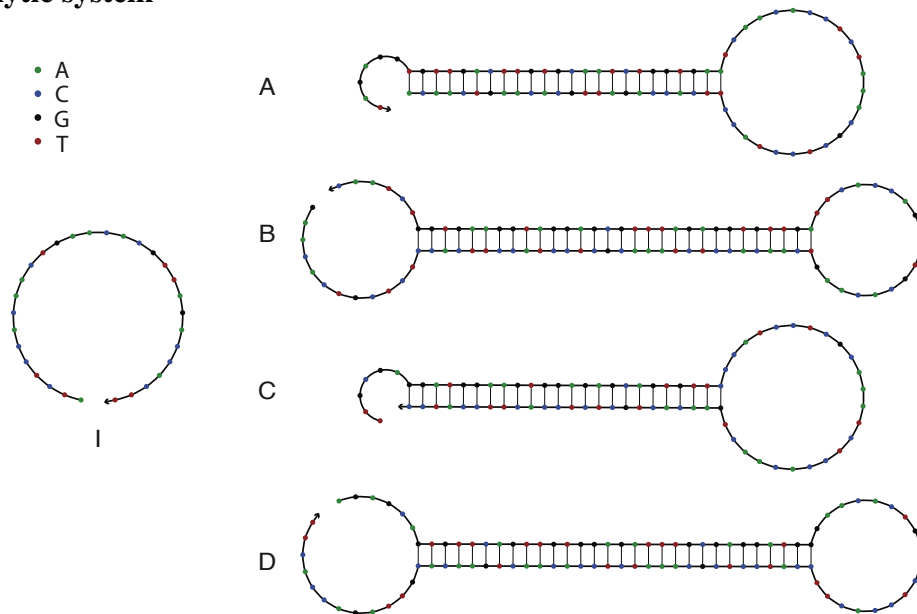


Figure S37. DNA sequences and secondary structures for the autocatalytic system of Fig. 3.

The sequences are also listed below as text sequences annotated with segment names.

A: x*-v*-b*-y*-u*-c*-a*-x*-y*-b*-v*-x*-a
 ACAACT-GAACAC-GTTAGA-CCACTT-CCATCC-TCGCAA-ATCTCC-ACAACT-AAGTGG-TCTAAC-GTGTTT-AGTTGT-GGAGAT

Aa-TET:
 /5TET/TT-ACAACTGAACACGTTAGACCACCTTCCATCCTCGCAAATCTCCACAACCTAAGTGGTCTAAC

Ab-BHQ1:
 /5Phos/GTGTTTCAAGTTGGAGAT/3BHQ_1/

B: v*-d*-y*-u*-c*-a*-x*-v*-b*-y*-x*-a*-c*-u*-y*-b
 GAACAC-TGCTCT-CCACTT-CCATCC-TCGCAA-ATCTCC-ACAACT-GAACAC-GTTAGA-CCACTT-AGTTGT-GGAGAT-TTGCGA-GGATGG-AAGTGG-TCTAAC

Ba:
 GAACACTGCTCTCCACTTCCATCCTCGCAAATCTCCACAACCTGAACACGTTAGACCACCTAGTTGTGGAGATTTGCGA

Bb:
 /5Phos/GGATGGAAGTGGTCTAAC

C: c*-u*-y*-d*-v*-u*-c*-a*-x*-v*-d*-y*-u*
 TTGCGA-GGATGG-AAGTGG-AGAGCA-GTGTTT-CCATCC-TCGCAA-ATCTCC-ACAACT-GAACAC-TGCTCT-CCACTT-CCATCC

Ca:
 TTGCGAGGATGGAAGTGGAGAGCAGTGTCCCATCCTCGCAAATCTCCACAACCTGAACACTGCTCTCC

Cb:
 /5Phos/ACTTCCATCC

D: d*-v*-x*-a*-c*-u*-v*-d*-y*-u*-c*-a*-x*-v*-b*-y*
 AGAGCA-GTGTTT-AGTTGT-GGAGAT-TTGCGA-GGATGG-GAACAC-TGCTCT-CCACTT-CCATCC-TCGCAA-ATCTCC-ACAACT-GAACAC-GTTAGA-CCACTT

Da:
 AGAGCAGTGTTCAGTTGTGGAGATTTGCGAGGATGGGAACACTGCTCTCCACTTCCATCCTCGCAAATCTCC

Db:
 /5Phos/ACAACTGAACACGTTAGACCACCTT

I: a*-x*-v*-b*-y*
 ATCTCC-ACAACT-GAACAC-GTTAGA-CCACTT

S8.4 Nucleated dendritic growth system

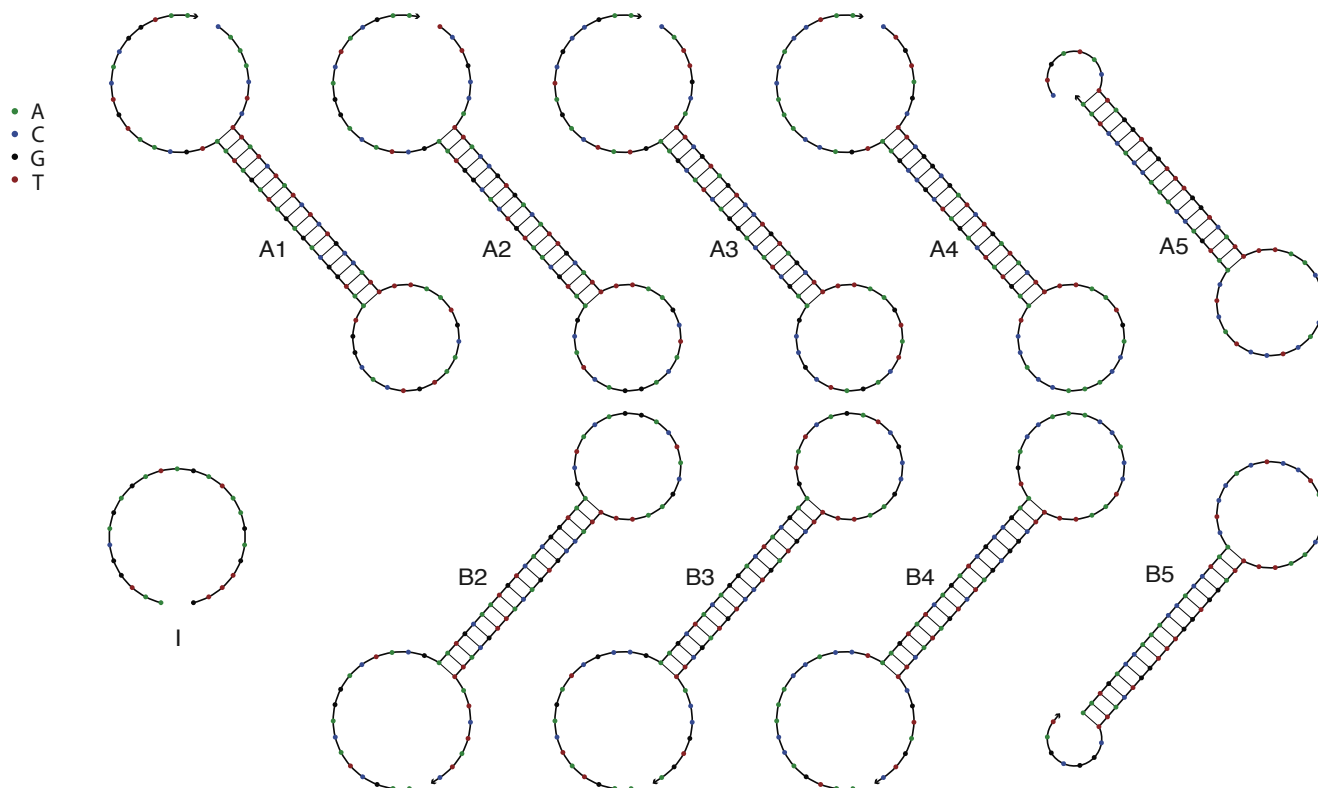


Figure S38. DNA sequences and secondary structures for the nucleated dendritic growth system of Fig. 4.

The sequences are also listed below as text sequences annotated with segment names. A1b-Cy5 (together with A1a) is used to synthesize Cy5 labeled hairpin A1.

A1: a-x-c-b-x-y-x*-d*-e*-x*-b*-c*-x*-d*-e*-x*
CAAAGTC-TT-ATCTATC-TCTGCCA-TT-TT-AA-TGCAATG-TCACGGT-AA-TGGCAGA-GATAGAT-AA-TGCAATG-TCACGGT-AA

A1a:
CAAAGTCCTTATCTATCTCTGCCATTTTAATGCAATGTCACGGTAATGGCAGA

A1b:
/5Phos/GATAGATAATGCAATGTCACGGTAA

A1b-Cy5:
/5Phos/GATAGATAATGCAATGTCACGGTAA-TT/3Cy5Sp/

A2: b-x-e-d-x-y-x*-f*-g*-x*-d*-e*-x*-f*-g*-x*
TCTGCCA-TT-ACCGTGA-CATTGCA-TT-TT-AA-GCTACAG-GACTACG-AA-TGCAATG-TCACGGT-AA-GCTACAG-GACTACG-AA

A2a:
TCTGCCATTACCGTGACATTGCATTTTAAGCTACAGGACTACGAATGCAATG

A2b:
/5Phos/TCACGGTAAGCTACAGGACTACGAA

A3: d-x-g-f-x-y-x*-h*-i*-x*-f*-g*-x*-h*-i*-x*
CATGCA-TT-CGTAGTC-CTGTAGC-TT-TT-AA-GTATCAG-ATCGCCG-AA-GCTACAG-GACTACG-AA-GTATCAG-ATCGCCG-AA

A3a:
CATGCAATTCGTAGTCCTGTAGCTTTTAAGTATCAGATCGCCGAAGCTACAG

A3b:
/5Phos/GACTACGAAGTATCAGATCGCCGAA

A4: f-x-i-h-x-y-x*-j*-k*-x*-h*-i*-x*-j*-k*-x*
CTGTAGC-TT-CGGCGAT-CTGATAC-TT-TT-AA-TGACCAA-ACCACCT-AA-GTATCAG-ATCGCCG-AA-TGACCAA-ACCACCT-AA

A4a:
CTGTAGCTTCGGCGATCTGATACTTTTAAATGACCAAACCACCTAAGTATCAG

A4b:
/5Phos/ATCGCCGAATGACCAAACCACCTAA

A5: h-x-k-j-x-y-x*-l*-m*-x*-j*-k*-x*
CTGATAC-TT-AGGTGGT-TTGGTCA-TT-TT-AA-CTCCACT-CCTACTC-AA-TGACCAA-ACCACCT-AA

A5a:
CTGATACTTAGGTGGT

A5b:
/5Phos/TTGGTCATTTTAACTCCACTCCTACTCAATGACCAAACCACCTAA

B2: x*-f*-g*-x*-d*-e*-x*-f*-g*-x*-y*-x-e-d-x-c
AA-GCTACAG-GACTACG-AA-TGCAATG-TCACGGT-AA-GCTACAG-GACTACG-AA-TT-TT-ACCGTGA-CATTGCA-TT-ATCTATC

B2a:
AAGCTACAGGACTACGAATGCAATG

B2b:
/5Phos/TCACGGTAAGCTACAGGACTACGAATTTTACCGTGACATTGCATTATCTATC

B3: x*-h*-i*-x*-f*-g*-x*-h*-i*-x*-y*-x-g-f-x-e
AA-GTATCAG-ATCGCCG-AA-GCTACAG-GACTACG-AA-GTATCAG-ATCGCCG-AA-TT-TT-CGTAGTC-CTGTAGC-TT-ACCGTGA

B3a:
AAGTATCAGATCGCCGAAGCTACAG

B3b:
/5Phos/GACTACGAAGTATCAGATCGCCGAATTTTTCGTAGTCCTGTAGCTTACCGTGA

B4: x*-j*-k*-x*-h*-i*-x*-j*-k*-x*-y*-x-i-h-x-g
AA-TGACCAA-ACCACCT-AA-GTATCAG-ATCGCCG-AA-TGACCAA-ACCACCT-AA-TT-TT-CGGCGAT-CTGATAC-TT-CGTAGTC

B4a:
AATGACCAAACCACCTAAGTATCAG

B4b:
/5Phos/ATCGCCGAATGACCAAACCACCTAATTTTCGGCGATCTGATACTTCGTAGTC

B5: x*-j*-k*-x*-l*-m*-x*-y*-x-k-j-x-i
AA-TGACCAA-ACCACCT-AA-CTCCACT-CCTACTC-AA-TT-TT-AGGTGGT-TTGGTCA-TT-CGGCGAT

B5a:
AATGACCAAACCACCTAACTCCACTCCTACTCAATTTTAGGTGGT

B5b:
/5Phos/TTGGTCATTCGGCGAT

I: x*-b*-c*-x*-a*
AA-TGGCAGA-GATAGAT-AA-GAGTTTG

S8.5 Fuel for the walker system

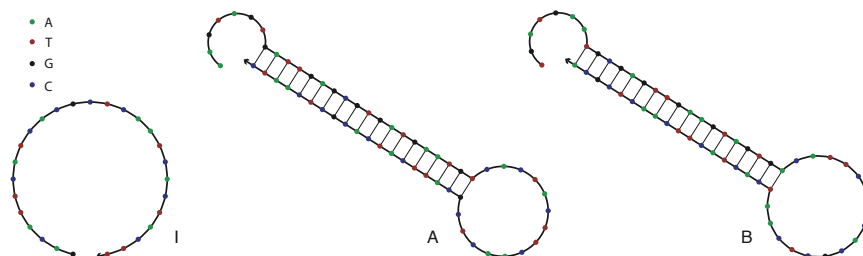


Figure S39. DNA sequences and secondary structures for the fuels for the walker system of Fig. S26 and Fig. S27.

The sequences are also listed below as text sequences annotated with segment names.

A: a-x-b-c-y-x*-a*-d*-y*-c*-b*-x*
 AAGTAGT-GA-TTGAGCG-TGATGAA-TG-TC-ACTACTT-CAACTCG-CA-TTCATCA-CGCTCAA-TC

Aa:
 AAGTAGTGATTGAGCGTGATGAATGTCACTACTTCAACTCGCATTTCATC

Ab:
 /5Phos/ACGCTCAATC

B: c-y-d-a-x-y*-c*-b*-x*-a*-d*-y*
 TGATGAA-TG-CGAGTTG-AAGTAGT-GA-CA-TTCATCA-CGCTCAA-TC-ACTACTT-CAACTCG-CA

Ba:
 TGATGAATGCGAGTTGAAGTAGTGACATTTCATCAGCTCAATCACTACT

Bb:
 /5Phos/TCAACTCGCA

I: x-y*-c*-b*-x*-a*
 GA-CA-TTCATCA-CGCTCAA-TC-ACTACTT

I-FAM:
 GACATTTCATCAGCTCAATCACTACTT/36FAM/

S8.6 Walker system

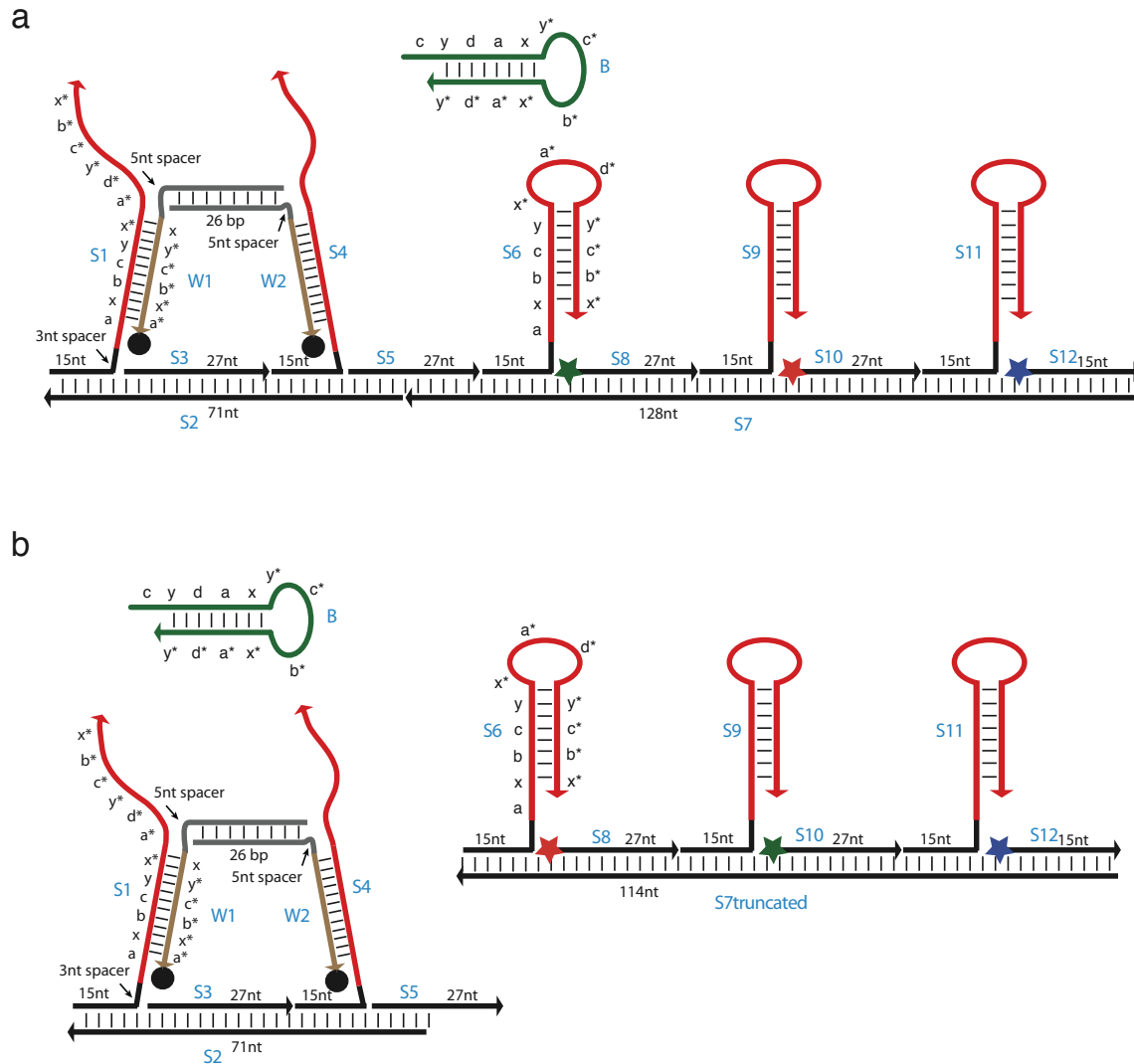


Figure S40. Secondary structure schematics for the walker system. a, Full track. **b**, Disjoint track for landing control experiments (Sect. S32). Blue letters indicate sequence names used in the definitions below. The lengths of segments a, b, c, and d are 7 nt; the lengths of segments x and y are 2 nt. Stars, fluorophores; black dots, quenchers.

Note:

- Sequence B is the same as that described in Sect. S8.5.
- W1s is used as a splint strand for ligating strands W1a and W1b to produce W1; W2s is used as a splint strand for ligating strands W2a and W2b to produce W2.

S1:
GGTAGTTCTAGGCAGCTGAAGTAGTGATGAGCGTGATGAATGTCCTACTTCAACTCGCATTTCATCAGCTCAATC

S1a:
GGTAGTTCTAGGCAGCTGAAGTAGTGATGAGCGT

S1b:
/5Phos/GATGAATGTCCTACTTCAACTCGCATTTCATCAGCTCAATC

S2:
TCATAGGCACCGTCAGACAGGATAGAGCAGTGATAGATAGTCATAGCCTTGGACCTGCCTAGAACTACC

S3:
GTCCAAGGCTATGACTATCTATGCACT

S4:
GCTCTATCCTGTCTGCTGAAGTAGTGATTGAGCGTGATGAATGTCCTACTTCAACTCGCATTTCATCAGCTCAATC

S4a:
GCTCTATCCTGTCTGCTGAAGTAGTGATTGAGCGT

S4b:
/5Phos/GATGAATGTCCTACTTCAACTCGCATTTCATCAGCTCAATC

S5:
ACGGTGCCTATGACATGGTACTCAGCT

S6:
GCTCGTATCTGGTCGCTGAAGTAGTGATTGAGCGTGATGAATGTCCTACTTCAACTCGCATTTCATCAGCTCAATC

S6a:
GCTCGTATCTGGTCGCTGAAGTAGTGATTGAGCGT

S6b:
/5Phos/GATGAATGTCCTACTTCAACTCGCATTTCATCAGCTCAATC

S7:
CGTAAAGTCGAGAGTATGCCATTGCCTCATCAGCGTAGCATCGAGATCTAAGTTAGTAACTCTGGCAGCCTGGTAGAGCGAGCCTATCGTCTGATGTACGACCAGA
TACGAGCAGCTGAGTACCATG

S7truncated:
CGTAAAGTCGAGAGTATGCCATTGCCTCATCAGCGTAGCATCGAGATCTAAGTTAGTAACTCTGGCAGCCTGGTAGAGCGAGCCTATCGTCTGATGTACGACCAGATACGAGC

S8-TMR:
/5TMRN/TACATCAGGACGATAGGCTCGCTCTAC

S8-JOE:
/5JOEN/TACATCAGGACGATAGGCTCGCTCTAC

S9:
CAGGCTGCCAGAGTTCTGAAGTAGTGATTGAGCGTGATGAATGTCCTACTTCAACTCGCATTTCATCAGCTCAATC

S9a:
CAGGCTGCCAGAGTTCTGAAGTAGTGATTGAGCGT

S9b:
/5Phos/GATGAATGTCCTACTTCAACTCGCATTTCATCAGCTCAATC

S10-TMR:
/5TMRN/ACTAACTTAGATCTCGATGCTACGCTG

S10-JOE:
/5JOEN/ACTAACTTAGATCTCGATGCTACGCTG

S11:
ATGAGGCAATGGCATTAGAAGTAGTGATTGAGCGTGATGAATGTCCTACTTCAACTCGCATTTCATCAGCTCAATC

S11a:
ATGAGGCAATGGCATTAGAAGTAGTGATTGAGCGT

S11b:
/5Phos/GATGAATGTCCTACTTCAACTCGCATTTCATCAGCTCAATC

S12-FAM:
/56FAM/ACTCTGCGACTTACG

W1:
TTGCCTCGTATCCTAACCGAACGGACTCCAGGACATTTCATCAGCTCAATCACTACTT

W1a:
TTGCCTCGTATCCTAACCGAACGGACTCC

W1b:
AGGACATTTCATCAGCTCAATCACTACTT /BHQ-1/

W1s:
CGTGATGAATGTCCTGGAGTCCGTTCCGGTT

W2 :
GTCCGTTTCGGTTAGGATACGAGGCAATCCAGGACATTCATCAGCTCAATCACTACTT

W2a :
GTCCGTTTCGGTTAGGATACGAGGCAATCC

W2b :
AGGACATTCATCAGCTCAATCACTACTT /BHQ-1/

W2s :
CGTGATGAATGTCCTGGATTGCCTCGTATC

References

1. Yurke, B., Turberfield, A.J., Mills, A.P., Jr., Simmel, F.C. & Neumann, J.L. A DNA-fuelled molecular machine made of DNA. *Nature* **406**, 605–608 (2000).
2. Turberfield, A.J. *et al.* DNA fuel for free-running nanomachines. *Phys. Rev. Lett.* **90**, 118102 (2003).
3. Bois, J.S. *Analysis of interacting nucleic acids in dilute solutions*. Phd, California Institute of Technology (2007).
4. Yurke, B. & Mills, Jr., A.P. Using DNA to power nanostructures. *Genet. Prog. Evol. Mach.* **4**, 111–122 (2003).
5. Behlke, M.A., Huang, L., Bogh, L., Rose, S. & Devor, E.J. Fluorescence and fluorescence applications. Tech. Rep., Integrated DNA Technologies (2005).
6. Devore, J.L. *Probability and Statistics for Engineering and the Sciences* (Brooks/Cole, 1991).
7. Behlke, M.A. & Devor, E.J. Chemical synthesis of oligonucleotides. Tech. Rep., Integrated DNA Technologies (2005).
8. Seeman, N.C. DNA in a material world. *Nature* **421**, 427–431 (2003).
9. Seeman, N.C. De novo design of sequences for nucleic acid structural engineering. *J. Biomol. Struct. Dyn.* **8**, 573–81 (1990).
10. Hofacker, I.L. *et al.* Fast folding and comparison of RNA secondary structures. *Chem. Mon.* **125**, 167–188 (1994).
11. Andronescu, M., Fejes, A.P., Hutter, F., Hoos, H.H. & Condon, A. A new algorithm for RNA secondary structure design. *J. Mol. Biol.* **336**, 607–624 (2004).
12. Dirks, R.M., Lin, M., Winfree, E. & Pierce, N.A. Paradigms for computational nucleic acid design. *Nucleic Acids Res.* **32**, 1392–1403 (2004).